



***This project has received funding from the European Union's Horizon 2020 research and innovation programme under the Marie Skłodowska-Curie grant agreement No 645704***

1     **Acoustic Emission behavior of thermally damaged Self-Compacting**  
2                     **High Strength Fiber Reinforced Concrete**

3  
4     **Hernán Xargay**

5     Comisión Nacional de Energía Atómica (CNEA), Departamento ICES, Buenos Aires, Argentina  
6     Universidad de Buenos Aires, Facultad de Ingeniería, INTECIN (UBA-CONICET), Argentina  
7     e-mail: [hernanxargay@cnea.gov.ar](mailto:hernanxargay@cnea.gov.ar)

8  
9     **Paula Folino**

10    Universidad de Buenos Aires. Facultad de Ingeniería. INTECIN (UBA-CONICET), Argentina  
11    e-mail: [pfolino@fi.uba.ar](mailto:pfolino@fi.uba.ar)

12  
13    **Nicolás Nuñez**

14    Comisión Nacional de Energía Atómica (CNEA), Departamento ICES, Buenos Aires, Argentina  
15    e-mail: [nnunez@cnea.gov.ar](mailto:nnunez@cnea.gov.ar)

16  
17    **Martín Gómez**

18    Comisión Nacional de Energía Atómica (CNEA), Departamento ICES, Buenos Aires, Argentina  
19    e-mail: [mpgomez@cnea.gov.ar](mailto:mpgomez@cnea.gov.ar)

20  
21    **Antonio Caggiano\***

22    Universidad de Buenos Aires. Facultad de Ingeniería. INTECIN (UBA-CONICET), Argentina  
23    Institut für Werksto im Bauwesen, Technische Universität Darmstadt, Germany  
24    e-mail: [acaggiano@fi.uba.ar](mailto:acaggiano@fi.uba.ar)

25  
26    **Enzo Martinelli**

27    Università di Salerno, Dipartimento di Ingegneria Civile, Fisciano (SA), Italy  
28    e-mail: [e.martinelli@unisa.it](mailto:e.martinelli@unisa.it)

29  
30    \*Corresponding Author.

31 **ABSTRACT**

32 This paper investigates the effect of high temperature on two different Self-Compacting (SC)  
33 cementitious composites. SC-High Strength (SCHSC) and Fiber-Reinforced Concrete (SCHSFRC)  
34 samples were tested in three-point bending after having been exposed to high temperature at 300 and  
35 600 °C. Besides the conventional force-displacement response, Acoustic Emission (AE) activity was  
36 monitored during the bending tests with the aim to investigate the possible correlation between the  
37 fracture behavior, the rate of AEs and the influence of high temperature exposure. The tests clearly  
38 pointed out the effects of heat exposure. More specifically, SCHSC specimens showed a significant  
39 decay in mechanical properties as a result of thermal treatment. Then, a lower degradation was  
40 observed for the SCHSFRC after heat exposure at 300°C, whereas the specimens exposed to 600 °C  
41 exhibited a tougher response than the corresponding SCHSC. The results showed that the effect of  
42 fibers played a beneficial role in bridging the expansion of heat-induced cracks developed in the  
43 concrete matrix during the exposure of specimens at high temperature. This bridging effect of fibers  
44 was observed also in terms of the AE activity: much less AE events were systematically registered  
45 for SCHSFRC specimens with respect to SCHSC ones, for a given value of the imposed Crack-  
46 Mouth-Opening-Displacement (CMOD). Therefore, AE measurements confirm their potential in  
47 scrutinizing the damage level in cementitious composites.

48

49

50 **KEYWORDS:** Acoustic Emission, Self-Compacting, High-Strength Concrete, Fiber-Reinforced  
51 Concrete, High Temperature.

## 52 1. INTRODUCTION

53 Over the last decades, the use of Self-compacting High-Strength Concrete (SCHSC) in the  
54 construction industry has been expanding considerably. Significant advances in new materials,  
55 quality and mixture proportioning, e.g. chemical admixtures and mineral binders, have led to both  
56 obtaining outstanding flowability at the fresh state and increasing compressive strength at the  
57 hardened state. As a result of the lower water-cement ratio, the microstructure of SCHSCs has less  
58 permeability and porosity, with enhanced durability against harmful actions of the environment,  
59 hence, a longer service life. However, strength increase implies a less ductile mechanical behavior  
60 [1][2]. The addition of amounts between 30 and 80 kg/m<sup>3</sup> of steel fibers in concrete improves its  
61 energy absorption capacity and limits the propagation and width of cracks [3]. SCHSC is also  
62 characterized by a higher content of cement paste and a more compact microstructure than those of  
63 Normal-Strength Concrete (NSC). Consequently, SCHSC could develop higher internal vapor  
64 pressure gradients under high-temperature exposure which allows to trigger microcracking and,  
65 sometimes, explosive detachment of parallel parts to the heated concrete surface. This phenomenon  
66 is called "spalling" and, although it can also occur in NSCs, it is more frequent and pronounced in  
67 High-Strength Concretes (HSCs) [4]. However, it was demonstrated that the incorporation of small  
68 amounts of polypropylene microfibers can partially mitigate this drawback [5][6][7].

69 The interest for investigating the behavior of concrete exposed to high temperatures has been  
70 motivated by two main reasons: fire resistance of tunnels and/or buildings and the nuclear facilities  
71 behavior. The design of new concrete demands to know their behavior under several environmental  
72 conditions, including for temperatures ranging between 20 °C and 800 °C [8][9]. Concrete exposed  
73 to high temperatures suffers chemical and physical changes, such as loss of moisture content,  
74 microstructure modification and aggregates decomposition which are mainly related to the reached  
75 maximum temperature of exposure [10]. Up to 200 °C no important changes take place in their  
76 mechanical properties due to the evaporation of the free and adsorbed water. Conversely, with

77 increasing temperature (up to 500 °C), the average pore size grows up due to the loss of water and  
78 dehydration of hydrated calcium silicates (C-S-H). Specifically, reaching 450 °C, the calcium  
79 hydroxide (Ca (OH)<sub>2</sub>) of the cement paste decomposes into calcium oxide (CaO<sub>2</sub>) and water. Up to  
80 these temperatures, the aggregates are more or less stable, excepting the siliceous aggregates.  
81 Furthermore, over 500 °C, concrete chemical and physical changes become very important and  
82 irreversible: at 573 °C, the aggregates  $\alpha$ -quartz crystalline phase transforms to  $\beta$ -quartz, resulting in  
83 deleterious expansions. A further increase in temperature up to 600 °C leads to the initiation of  
84 chemical decomposition in C-S-H, which is the main strengthening compound of cementitious  
85 matrix. Between 600 °C and 800 °C calcium carbonate (CaCO<sub>3</sub>) dissociates. Moreover, after 800°C  
86 all the hydration or chemically combined water has already been lost and the strength capacity  
87 becomes very low. Finally, at 1200 °C the solid compounds begin to melt [11]. However, concrete  
88 behavior subjected to high temperature does not only depend on the maximum temperature, but it is  
89 also affected by many environmental conditions, such as heating rate, temperature permanence time,  
90 cooling and humidity level, among others [9][10][12].

91 Several investigations have shown that thermal actions induce substantial modifications in  
92 cohesion and strength of concrete, which reduce both Young's modulus and Poisson's coefficient  
93 [13][14][15][16][17]. Concrete behaves in a more ductile manner increasing peak compressive  
94 strength deformation as temperature rises [18]. In addition, a slight increase in fracture energy  
95 released up to 400 °C has been observed, which decreases at higher temperature due to excessive  
96 thermal damage and the strong loss of tensile and compression strength [19][20]. Specifically, the  
97 experimental evidence for Self-Compacting Concrete (SSC) at high temperature shows that their  
98 mechanical properties are more seriously thermally degraded than traditionally-vibrated ones  
99 [17][21] [22][23][24].

100 The actual state of damage of concrete can be scrutinized by means of non-destructive  
101 techniques, among which Acoustic Emission (AE) testing is gaining consensus within the scientific

102 community [25]. In fact, AE is known as the spontaneous release of elastic energy in the form of  
103 transient elastic waves that occurs within the materials when are stressed [26]. Hence, the waves  
104 contain information about internal behavior of the material [27]. Structural modifications such as  
105 cracks growth and friction are generated as the fracture process of concrete is progressing, which are  
106 associated with acoustic emissions. These elastic waves propagate from their sources to the surface  
107 where piezoelectric sensors convert them into electrical signals which can be subsequently processed  
108 by a specific electronic equipment. A set of relevant signal parameters can be calculated in order to  
109 characterize the digitalized AE waveforms. Therefore, AE technique has been used to monitor in real  
110 time laboratory mechanical tests of concrete specimens due to it great sensitivity to detect damage  
111 evolution from the very beginning [28][29][30][31][32]. Many investigations have been carried out  
112 in order to quantify the global damage level of reinforced concrete elements using AE-based  
113 parametric approaches. For this purpose, new indexes derived from conventional AE parameters have  
114 been defined: e.g., the Calm ratio [33][34], the Cumulative Signal Strength ratio [35][36], Relaxation  
115 ratio [37], b-value [38][39][40] and the Improved b-value [41], among others. Moreover, AE can  
116 deliver useful information to detect, locate and infer the origin of the sources [30][42][43]. In this  
117 regard, several experimental results have been reported evidencing the close relationship between the  
118 AE features with the source cracking mode [44][45][46][47]. It has been pointed out that tensile  
119 fracture mode, characterized by opening movements of the crack, results in AE signals with higher  
120 frequency and shorter rise time (defined as elapsed time from the first arrival to the peak amplitude).  
121 On the other hand, shear fracture mode waveforms, represented by a sliding movement of the crack  
122 faces, show lower frequency and longer rise time and duration. Thus, AE events can be plotted in a  
123 bi-dimensional representation defined by the combined features of the RA value (rise time over  
124 amplitude) and the Average Frequency (AF) (counts over duration) to assess the cracking mode  
125 corresponding to the AE source.

126 This work reports the results obtained from three-point bending tests carried out on both  
127 SCHSC and SCHSFRC with the aim to investigate the influence of heat-induced damage on their  
128 cracking and post-cracking behavior. Both force-displacement relationship and AE activity were  
129 monitored during those tests. Thermal treatments were performed in an electric furnace at maximum  
130 temperatures of 300 and 600 °C. Steel macrofibers (0.76% in volume) and polypropylene microfibers  
131 (0.1%) were dispersed within the concrete matrix of the SCHSFRC mixture. It is important to remark  
132 that the adopted methods followed in this work mainly investigated the high temperature exposure at  
133 the material level and thus, the structural response at a fire scenario is out of the scope of this paper.

134 It is worth highlighting that, in the Authors' best knowledge, no experimental research is  
135 available in the scientific literature reporting the fracture behavior and AE activity of thermally  
136 damaged SCHSFRC and tested in bending. Indeed, the exiguous related results currently available  
137 refer to either Fiber Reinforced Concrete (FRC) [48][49][50][51], or thermally-treated concrete  
138 without steel fibers reinforcement [52][53][54][55]. Therefore, the results presented in this paper  
139 could be useful to researchers interested at studying the AE applicability limits as valuable tool in  
140 Structural Health Monitoring (SHM) for high responsibility structures, such as spent nuclear fuel  
141 storage facilities.

## 142 2. MATERIALS AND METHODS

143 This section summarizes the experimental activities related to the AE tests executed at the Laboratory  
144 of Materials and Structures of the University of Buenos Aires, Argentina. Further details on the  
145 extended experimental program and results of complementary mechanical tests can be found in [56].  
146 The specimens for this experimental program were prepared adopting a unique dosage for the  
147 concrete matrix characterized by a water-to-binder ratio of 0.35. This mixture was designed to achieve  
148 an adequate flowability at the fresh state and at the same time a high-strength in hardened state.  
149

### 150 2.1. Materials

151 The selected concrete constituents were early age high-strength Portland cement, finely ground  
152 granulated blast furnace slag (GGBFS), three different fractions size of siliceous aggregates and a  
153 very high range polycarboxylate-based superplasticizer admixture. The mixture composition is  
154 detailed in Table 1. The maximum nominal size of the coarse fraction was  $\Phi_{\max} = 9.50$  mm and the  
155 overall Fineness Modulus (FM) resulting from the total aggregate mixture was  $FM = 4.29$ . The  
156 SCHSC mean uniaxial compressive strength was 97.9 MPa, obtained from three cylinders of 100 mm  
157 diameter and 200 mm height.

158 According to their length, fibers for concrete are usually classified in micro and macrofibers.  
159 The former are used to reduce drying shrinkage and to prevent the spalling effect, while macrofibers  
160 increase the ductility and restrict the growth of macrocracks [57]. In this research, FibroMac 12  
161 monofilament polypropylene microfibers (0.1% in volume) and Wirand FS3N steel macrofibers  
162 (0.76% in volume) were used (*Figure 1*). Main technical data for both fibers are shown in Table 2.

163 The following labels were adopted based on the concrete composition and maximum  
164 temperature exposure:

- 165 - SCHSC20: plain concrete, without exposure to high temperature;
- 166 - SCHSC300: plain concrete exposed to 300 °C;



- 167 - SCHSC600: plain concrete exposed to 600 °C;
- 168 - SCHSFRC20: fiber-reinforced concrete, without exposure to high temperature;
- 169 - SCHSFRC300: fiber-reinforced concrete exposed to 300 °C;
- 170 - SCHSFRC600: fiber-reinforced concrete exposed to 600 °C.

## 171 **2.2. Methods**

172 Concrete batches were realized in a laboratory pan type concrete mixer with vertical axis. Three  
173 beams (150 x 150 x 600 mm<sup>3</sup>) were molded for each concrete batch. Due to self-compacting  
174 characteristics, molds were filled in a single pour and no further compaction was carried out. The  
175 specimens were thus demolded after 24 hours and cured until 28 days-age immersed in water at 20  
176 °C temperature. Subsequently, they were stored in laboratory conditions for moisture stabilization up  
177 to heat treatment.

178 The concrete specimens set SCHSC300, SCHSC600, SCHSFRC300 and SCHSFRC600 were  
179 individually subjected to 300 and 600 °C maximum temperature in a vertical electric oven for 3 hours  
180 (*Figure 2a*). The adopted heating rate (*Figure 2b*) was 10 °C / min. Then, cooling was done slowly  
181 into the furnace and were removed 24 hours later. Spalling phenomena never occurred, however,  
182 numerous cracks were observed on the surface of the treated samples, especially for those heated at  
183 600 °C. Nevertheless, fiber-reinforced concrete specimens showed better surface integrity. All the  
184 specimens were weighted immediately before and after the heat treatments. The mean relative weight  
185 loss was 6.8% for SCHSC300, 6.7% for SCHSFRC300, 8.0% for SCHSC600 and 8.2% for  
186 SCHSFRC600. It is concluded that the effect of the addition of fibers in weight loss was totally  
187 negligible. These results are in agreement with those reported by [21], where two different mixtures  
188 of SSC were treated at a heating rate of 1 °C / min.

189 After the aforementioned operation a notch of 25 mm deep were cut at mid-span of the beams  
190 with a diamond-edged saw. Then, the flexural behavior was evaluated in three-point bending test  
191 (TPB) 30 days after heat treatments by means of a 2000 kN maximum capacity testing machine with

192 closed-loop control according to RILEM TC 162-TDF recommendations [58]. The beam span was  
193 500 mm and load was applied in central notched section. Test control was performed by means of a  
194 Crack Mouth Opening Displacement (CMOD) feedback-control. CMODs were measured through a  
195 clip gauge sensor with the aim of characterizing the post-peak tensile behavior. The CMOD rate was  
196 0.05 mm/min until 0.25 mm reading was reached and then 0.20 mm/min up to the test end. Load  
197 measurement was performed by a 300 kN capacity load cell.

198 The tests were continuously monitored by AE testing system. For this purpose, a PAC AE  
199 system PCI-2 board with two R15D 150 kHz resonant sensors and 2/4/6 preamplifiers with 40 dB  
200 gain were used. Although for field inspections in real structures, and with large separation/distance  
201 between the sensors, it is widely recommended to use low frequency resonant sensors, 150 kHz  
202 sensors were used in this experimental campaign for two main reasons: (a) the specimens and  
203 distances between the sensors were small, thus, the crack tip were in the range of 6-17 cm, and (b)  
204 sensors with 150 kHz resonant frequency are more adequate to supply good sensitivity and to reduce  
205 background noise. Moreover, the used sensors with external preamplifier are more sensitive than low  
206 frequency resonant sensors with included preamplifier. Thus, the choice of using 150 kHz sensors  
207 was the result of a balance between the sensitivity and attenuation for this particular experimental  
208 setup.

209 The sensors were symmetrically located at 5 cm of each side the notch axis on the bottom  
210 surface of the beam as shown in *Figure 3*. Rubber acoustic insulations were placed at the support in  
211 order to reduce friction noise. Vaseline as coupling media at sensors-concrete interface was used.  
212 Before performing each flexural test, preliminary measurements of the background noise and signal  
213 attenuation trials were carried out, for the later by generating Hsu-Nielsen artificial sources at  
214 different points on the beam front surface. A measurement threshold of 45 dB and a frequencies filter  
215 of 20-400 kHz were preset in the equipment. The AE adopted sampling frequency was 2 MHz. In  
216 order to extract spurious hits without physical sense, AE raw data were firstly pre-filtered by

217 magnitude of AE features. Then, to corroborate that emission sources were generated at the central  
218 volume of the beams, data were filtered by a zone location criterion based on time of arrival. For the  
219 specimens treated at 600 °C, it was found that the isotropic medium hypothesis (apparent wave  
220 velocity) did not provide accurate results due to high amounts of inhomogeneous thermal damages.  
221 Hence, in those cases, only the magnitude of AE features was used for data filtering.  
222

## 223 3. RESULTS AND DISCUSSION

### 224 3.1 Mechanical performance

225 Figures 4, 5 and 6 show the Load-CMOD behavior for the reference temperature and thermal  
226 treatments at 300 °C and 600 °C, respectively. In each graph, the black line represents the average  
227 response of the three tests, while the gray envelope area indicates the experimental scatter. The fibers  
228 random distribution and cracks induced by thermal conditioning are some of several factors, besides  
229 the natural heterogeneity of concrete behavior, which contribute with the dispersion of results.

230 As expected, the presence of fibers results in a much higher toughness of the SCHSFRC with  
231 respect to SCHSC (*Figure 4*). Conversely, the pre-peak branch and the cracking strength, which are  
232 mainly related to the matrix properties, were almost unaffected by the presence of fibers, as they  
233 mainly start working after the cementitious matrix cracking [59]. It is also observed that the maximum  
234 CMOD achieved was less than 1.5 mm for SCHSC20, contrarily in the case with fibers, the beams  
235 still had load bearing capacity even for 3.0 mm at the end of the test.

236 Peak load reduces for 300 °C maximum temperature treatment especially when plain concrete  
237 specimens (SCHSC300) were analyzed. Conversely, the bridging action of fibers is still effective, as  
238 specimens SCHSFRC300 exhibited a barely plastic response, though with a lower cracking strength  
239 due to the heat-induced degradation in the concrete matrix (*Figure 5*).

240 Finally, a strong degradation of the mechanical behavior can be observed in the case of  
241 specimens pre-exposed to 600°C (*Figure 6*). On the one hand, two out of three SCHSC specimens  
242 failed abruptly at peak load for plain concrete and, therefore, it can be said that 600°C is an extreme  
243 temperature for plain SCHSC. Fracture occurred near the notches through preexisting thermal cracks,  
244 in both cases for CMOD less than 0.25 mm, resulting in a very low energy absorption capacity. Hence,  
245 only one complete result on SCHSC600 including post peak is reported in *Figure 6*: its flexural  
246 strength is about 15% of the one average determined for SCHSC20. On the other hand, all  
247 SCHSFRC600 specimens behaved in a similar manner, though their cracking strength was about 20%

248 of SCHSFRC20 and the bridging effect of fibers was much weaker than in the other cases (20 and  
249 300 °C).

250 In order to characterize and compare the tensile behavior of fiber-reinforced concretes, the  
251 RILEM recommendation TC 162-TDF defines representative flexural parameters that can be  
252 obtained from the Load-CMOD curve. These parameters are: the flexural strength  $f_{ct,L}$  (corresponding  
253 to the highest value of the load ( $F_L$ ) in the range of CMOD 0.05 mm), the energy absorption capacity  
254 due to the plain concrete  $D_{BZ}^b$ , the energy absorption capacity due to the influence of fibers  $D_{BZ,2}^f$   
255 and  $D_{BZ,3}^f$ , the equivalent flexural tensile strength ( $f_{eq,2}$  and  $f_{eq,3}$ ) and the residual flexural tensile  
256 strength  $f_{R,1}$  (CMOD=0.5),  $f_{R,2}$  (CMOD=1.5) and  $f_{R,3}$  (CMOD=2.5). In structural engineering  
257 applications,  $f_{R,1}$  is accepted to be relevant for the serviceability limit state while  $f_{R,3}$  is related with  
258 the ultimate limit state. Table 3 summarizes the flexural parameters aforementioned. For the case of  
259 plain concrete, the fracture energy  $G_f$  was calculated following RILEM recommendation TC 50-FCM  
260 [60] and  $D_{BZ}^b$  was evaluated as the total area under the Load-CMOD curve.

261 *Figure 7* shows two X-ray images corresponding to the same sample and rotated 90 degrees.  
262 The specimen used for this descriptive purpose (75 x 75 x 250 mm<sup>3</sup>) was sawn from one beam after  
263 been tested to make it compatible with the portable X-ray equipment. The images revealed that the  
264 fibers are uniformly distributed in the concrete matrix despite being a self-compacting concrete.  
265 Preferential orientations are only observed in the vicinity of the specimen faces that were in contact  
266 with the steel mold.

267 *Figure 8* shows photographs of the resulting failure faces and paths in three-point bending tests  
268 for SCHSC and SCFRHSC. Visual inspection of fracture surfaces of SCHSC specimens (*Figure 8a*)  
269 allowed distinguishing color changes related with maximum temperature of exposure. Granitic coarse  
270 aggregate shifted from dark bluish-grey at 20 °C and 300 °C to a lighter shade of grey, pink and white  
271 at 600 °C. Meanwhile, mortar phase color varied from normal grey to yellowish-grey at 300 °C and  
272 to darker grey at 600 °C with a remarkable increasing of porosity and friability. Another temperature

273 effects can also been detected on the fracture surfaces: at 20 °C and 300 °C the cracks fractured the  
274 aggregates while at 600 °C cracks go mainly through the interface between cement paste and  
275 aggregates, as it is usually occurring in non-thermally damaged NSC. From Figure 8b and 8c, it can  
276 be highlighted that the tortuosity of crack paths was increased with temperature for both SCHSC and  
277 SCHSFRC. Moreover, for SCHSFRC600 the matrix stiffness weakening and the fibers bridging  
278 action generated several path direction changes, ensuring structural integrity of the specimens.

### 279 **3.2 AE energy behavior**

280 In the following “AE energy” refers to the Measured Area under the Rectified Signal Envelope  
281 (MARSE). The AE energy evolutions for the three thermal scenarios are shown in Figure 9, 10 and  
282 11. Again, the average response of three tests repetitions with their dispersion is presented, with the  
283 exception of SCHSC600 as was explained before. Similar tendencies were observed in the cumulative  
284 curves corresponding to different AE parameters such as Counts, Duration, Amplitude and Signal  
285 Strength when expressed in their relative values. The AE energy is often selected to represent the  
286 magnitude of source event rather than other AE parameters (e.g. hits) because it is a function of both  
287 duration and amplitude of the signal. Furthermore, it is also less sensitive on threshold setting and  
288 operating frequency [61]. For the sake of brevity, only the cumulative AE energy as representative  
289 parameter of one channel is presented in this subsection. It can be noticed that AE results dispersion  
290 was increased with temperature. Thermal cracks were randomly distributed along the specimens and  
291 it greatly affected the fracture path development.

292 Figure 12 shows the average Load-CMOD curve with the average cumulative AE energy  
293 response for the SCHSC20 and SCHSFRC20 specimens. Similarly, Figures 13 and 14 reproduce the  
294 concretes performance after the heat treatments. Very few AE energy was recorded during the pre-  
295 peak branch in comparison to the post-peak (softening) branch for the cases of reference temperature,  
296 i.e. 20 °C (Figure 12). This behavior can be explained due to microcracks growth in the intact cement  
297 matrix which are very low in comparison with the macrocracks localization development.

298 Nevertheless, for SCHSFRC300 this behavior is quite different. Figure 13 highlights that already a  
299 30% of the AE energy recorded during the tests were released before reaching the maximum load. It  
300 seems that the fibers action greatly contributes to withstand the loss of cohesion of the matrix due to  
301 the thermal degradation and increase the bearing capacity of the beam.

302 In all temperature scenarios, the AE rate is higher in plain concrete, reaching towards the test  
303 end with similar cumulative amounts. Therefore, for different CMOD values less than 2.0 mm, the  
304 cumulative AE is higher in SCHSC than in SCHSFRC. In the Authors understanding, this  
305 phenomenon was due to the fact that when applying a given CMOD, the fibers oppose to growing  
306 and coalescence of microcracks and, hence, less AE is released in SCHSFRC than in plain concrete.  
307 This is in good agreement with the conclusion by Rossi et al. [62], since they evidenced that the  
308 localized forces due to steel fibers mainly helps to delay the formation of microcracks, but they cannot  
309 prevent it. Cumulative AE curve slope flattens as the cracking develops in concrete matrix. However,  
310 AE continued to be recorded due to the friction caused by the interworking of the aggregates, the  
311 interaction between the new surfaces of the matrix and the fibers pullout mechanisms. AE behavior  
312 during CMOD controlled tests is significantly different from that typically observed in plain concrete  
313 where test control is performed through stroke displacement [49][50][55]. In such tests, plain  
314 specimens abruptly fail when the maximum load is reached, generating an instantaneous large amount  
315 of AE activity.

316 Taking into account that concrete serviceability limit states design rules restrict crack openings  
317 up to a maximum of 0.40 mm for environmental normal exposure [63], the amount of cumulative AE  
318 that can be related to concrete damage level, was significantly lower for SCHSFRC than for SCHSC.  
319 This means that, after crack opening, fibers are capable to “delay” the cracking process development  
320 throughout the concrete matrix. This concept can be thus identified with the AE technique.

321 Concrete samples after 600 °C showed comparatively lower AE amount and amplitude  
322 especially at the beginning stage of the tests. In those tests, the inner structure of the specimens was

323 degraded and had multiple cracks as result of the thermal treatment and, therefore, an important  
324 irreversible release of internal energy manifested as AE [52]. Then, when testing the beams, such  
325 energy is no longer available. Moreover, preexisting thermal cracks dampen the propagation of AE  
326 waves through the material and, hence, attenuate AE signals.

327 Finally, Figures 15 and 16 aim at further highlighting the effect of temperature on the bending  
328 response of the two series of specimens of SCHSC and SCHSFRC. Specifically, Figure 15 shows  
329 that the elastic response of SCHSC300 is almost overlapped to the one of the reference material. AE  
330 keep producing in the post elastic range for SCHSC300, as a more gradual cracking process develops  
331 in these specimens due to the preexistence of heat-induced micro-cracks that progressive coalesce  
332 during the loading process. Conversely, the extremely weak response observed for SCHSC600 leads  
333 to few AE events, as the heat-induced micro-cracks have already severely weakened the concrete  
334 matrix continuity.

335 The obtained results of cumulative total amount of AE energy seem to showed a direct  
336 correlation with the fracture energy in plain concrete. Related to the reference case (20 °C), the  
337 fracture energy increased 44% at 300 °C due to greater tortuosity of the fracture and decreased 34%  
338 at 600 °C due to the severe thermal damages (Table 3). This behavior is in agreement with the  
339 conclusions reported by some authors in literature [19][20]. On the other hand, the total AE energy  
340 grew 50% at 300 °C and reduced 93% at 600 °C.

341 Figure 16 illustrates that fibers are capable to make cracking process almost overlapped for  
342 SCHSFRC20 and SCHCFRC300; however, the response of SCHSFRC600 is significantly affected  
343 by heat-induced damage, as already observed for SCHSC600 specimens. In opposition with plain  
344 concrete, SCHCFRC do not presented a clear relationship between AE energy and energy absorption  
345 capacity.

346 Finally, it is remarked that no comparisons can be proposed with other results available in the  
347 literature. To the Authors' best knowledge, other available data are obtained from tests carried out by



348 different experimental procedures. Specifically, some results correspond to different mechanical  
349 tests, others to non-thermally treated specimens and, in most of the cases, to different AE equipment  
350 layouts and/or experimental setups.

### 351 *3.3 AE frequency and RA value evolutions*

352 Figure 17 shows the histograms of RA value vs. average frequency of AE hits for all the  
353 analyzed concrete mix composition and temperature scenarios. The moving average of the RA value  
354 and the average frequency of 100 hits have been represented in order to smooth out scattering. The  
355 adopted criterion for a moving average of 100 hits was chosen as result of a previous sensitive study  
356 on AE data analysis. Trial examples performed with 25, 50, 75, 100, 150 and 200 hits were done. It  
357 was found that the plotted data become smooth and stable from 100 hits. This is also in accordance  
358 with RILEM TC 212-ACD [64] that recommends the adoption of more than 50 hits.

359 The plots distribution indicates that as the temperature grows up, the AE events decrease in  
360 frequency and increase in RA. This can be visualized by the progressive displacement of the AE  
361 cluster to the right and down corner in the figures. The tendency is evidenced both in SCHSC and  
362 SCHSFRC, and clearly point out that as concrete thermal degradation is more severe, the cracking  
363 behavior shifts to more mixed fracture modes. This is consistent with the observed increasingly  
364 tortuous fracture morphology.

365 Moreover, if the effect of the incorporation of fibers is analyzed, an increase of the RA value  
366 and the AF (although slightly in this case) is observed. This indicates that the fibers tend to modify  
367 the cracking modes activating the mixed modes as well. This was also supported by the fracture  
368 pattern aforementioned. Finally, Figure 18 illustrates this behavior representing the peak frequency  
369 distribution of AF and RA value.

#### 370 4. CONCLUSIONS

371 Self-compacting high strength concrete samples with and without hybrid steel/polypropylene fibers  
372 have been investigated in this work. Specifically, test specimens were exposed to maximum  
373 temperatures of 300 and 600 °C and, then, tested in bending. Both load-displacement response and  
374 AE activity were monitored during those tests.

375 On the one hand, the mechanical behavior allows to establish the following concluding remarks:

- 376 - peak flexural strength is significantly affected by temperature, though the fiber  
377 reinforcement shifts the residual flexural behavior;
- 378 - a remarkable nonlinearity can be observed in the bending response, as a consequence of  
379 matrix stiffness degradation due to high temperatures exposures;
- 380 - the fracture energy of SCHSC slightly increased for 300 °C and strongly decreased for 600  
381 °C samples;
- 382 - fiber-reinforced concrete specimens continued to have considerable residual energy  
383 absorption capacity after the heat treatment, even at 600 °C.

384 On the other hand, AE measurements highlighted the following remarks:

- 385 - the bridging action of fibers restrain cracks propagation, which results in cumulative AE  
386 energy being released in SCHSFRC also during advanced stages of the post-cracking  
387 response and CMOD values;
- 388 - load-induced macro-cracks that are generated from pre-existing heat-induced micro-cracks,  
389 produce in SCHSFRC a smaller amount of AE hits with smaller amplitude than in plain  
390 specimens;
- 391 - in SCHSC, the recorded cumulative AE energy relatively grew up from 20°C to 300°C and  
392 declined for 600°C as a result in the change of fracture energy due to heat-exposure;
- 393 - although the incorporation of fibers increased considerably the energy absorption capacity,  
394 the AE energy did not grow within the analyzed CMOD ranges, these latter chosen as  
395 representative for the useful life of a concrete structure;

- 396 - increasing thermal damages shifted the cracking modes to shear and mixed modes,  
397 characterized by a progressive decrease in average frequency and increase in RA value;
- 398 - incorporation of fibers in concrete slightly affects the AE features, changing to mixed  
399 modes, mainly increasing the RA values;
- 400 - advanced stages of cracking, produced by both thermal and mechanical process, constitute  
401 a limitation to the application of AE, as cracks dampen the AE signals.

402 Finally, the experimental results obtained from this study confirm the promising non-destructive AE  
403 technique for scrutinizing the actual level of damage. Analysis of different concrete composites,  
404 possible subjected to high temperature exposures and with fiber reinforcements were deeply  
405 investigated. Future research steps will aim at extending this procedure to other stress state conditions  
406 (i.e., uniaxial compression, triaxial compression and mixed modes of fracture) and to  
407 calibrate/connect the AE measurements together with the fracture mechanics parameters employed  
408 in a constitutive model capable to predict the stress-crack opening displacements of FRC beams  
409 exposed to high temperatures.

410

411

412

413 **ACKNOWLEDGEMENTS**

414 Contribution from the staff of the Laboratory of Materials and Structures of the University of  
415 Buenos Aires (UBA) is gratefully acknowledged, particularly Dr. L. Fernandez Luco for his valuable  
416 advices. Also, the authors are grateful to Eng. G. Fornasier (Lomax-InterCement) for providing raw  
417 materials, Eng. L. Sambataro for his collaboration with the experimental program and Eng. J.  
418 Scopelliti and E. Olivar Godaz (CNEA-ENDE) for the x-ray images.

419 The financial support of the “National Atomic Energy Commission of Argentina” (CNEA) and  
420 the SUPERCONCRETE Project ([www.superconcrete-h2020.unisa.it](http://www.superconcrete-h2020.unisa.it)), funded by the European  
421 Union (Horizon 2020 Program, MSCARISE-2014, No. 645704) are also acknowledge. The  
422 Alexander von Humboldt-Foundation is also acknowledged for funding the temporary research  
423 position of Dr. A. Caggiano at the Institute of Construction and Building Materials - TU-Darmstadt  
424 under the research grant ITA-1185040-HFST-(2CENENRGY project).

425 **REFERENCES**

- 426 [1] ACI Committee 363 - ACI 363R-10. (2010). Report on High-Strength Concrete. Reported by  
427 ACI Committee 363.
- 428 [2] Martinelli, E., Caggiano, A., Xargay, H. (2015). An experimental study on the post-cracking  
429 behaviour of Hybrid Industrial/Recycled Steel Fibre-Reinforced Concrete. *Construction and Building*  
430 *Materials*, 94, 290-298.
- 431 [3] ACI Committee 544 - ACI 544.1R-96. (Reapproved 2009). State-of-the-Art Report on Fiber  
432 Reinforced Concrete. Reported by ACI Committee 544.
- 433 [4] Castillo, C., Durrani, A.J. (1990). Effect of Transient High Temperature on High-Strength  
434 Concrete. *ACI Materials Journal*, 87, 47-53.
- 435 [5] Han, C.-G., Hwang, Y.-S., Yang, S.-H., Gowripalan, N. (2005). Performance of spalling  
436 resistance of high performance concrete with polypropylene fibers contents and lateral confinement.  
437 *Cement and Concrete Research*, 35(9), 1747-1753.
- 438 [6] Noumowe, A. (2005). Mechanical properties and microstructure of high strength concrete  
439 containing polypropylene fibres exposed to temperatures up to 200 °C. *Cement and Concrete*  
440 *Research*, 35(11), 2005.
- 441 [7] Behnood, A., Ghandehari, M. (2009). Comparison of compressive and splitting tensile strength  
442 of high-strength concrete with and without polypropylene fibers heated to high temperatures. *Fire*  
443 *Safety Journal*, 44(8), 1015-1022.
- 444 [8] RILEM Technical Committee 200-HTC: Mechanical concrete properties at high temperatures  
445 – modelling and applications. Part 1: Introduction – General presentation. (2007). *Materials and*  
446 *Structures*, 40, 841-853.
- 447 [9] Naus, D.J. (2010). A compilation of elevated temperature concrete material property data and  
448 information for use in assessments of nuclear power plant reinforced concrete structures  
449 (NUREG/CR-7031). US Nuclear Regulatory Commission, Washington.
- 450 [10] Houry, G.A. (2000). Effect of fire on concrete and concrete structures. *Progress in Structural*  
451 *Engineering and Materials*, 4(2), 429-447.
- 452 [11] Arioz, O. (2007). Effects of elevated temperatures on properties of concrete, *Fire Safety*  
453 *Journal*, 42(8), 516-522.
- 454 [12] Phan, L., Carino, N. (2002). Effects of test conditions and mixture proportions on behavior of  
455 high-strength concrete exposed to high temperatures. *ACI Materials Journal*, 99(1), 54-66.
- 456 [13] Marechal, J.C. (1972). Variations in the modulus of elasticity and Poisson's ratio with  
457 temperature. *ACI Special Publication* 34, 495-504.
- 458 [14] Janotka, I., Bagel, L. (2002). Pore structures, permeabilities, and compressive strengths of  
459 concrete at temperatures up to 800 °C. *ACI Materials Journal*, 99(2), 196-200.
- 460 [15] Lee, J., Xi, Y., Willam, K. (2008). Properties of concrete after high-temperature heating and  
461 cooling. *ACI Materials Journal*, 105(4), 334-341.
- 462 [16] Zhang, B. (2011). Effects of moisture evaporation (weight loss) on fracture properties of high  
463 performance concrete subjected to high temperatures. *Fire Safety Journal*, 46(8), 543-549.

- 464 [17] Pineaud, A., Pimienta, P., Rémond, S., Carré, H. (2016). Mechanical properties of high  
465 performance self-compacting concretes at room and high temperature. *Construction and Building*  
466 *Materials*, 112, 747-755.
- 467 [18] Chang, Y.F., Chen, Y.H., Sheu, M.S., Yao, G.C. (2006). Residual stress-strain relationship for  
468 concrete after exposure to high temperatures. *Cement Concrete Research*, 36(10), 1999-2005.
- 469 [19] Baker, G. (1996). The effect of exposure to elevated temperatures on the fracture energy of  
470 plain concrete. *Materials and Structures*, 29(19), 383-388.
- 471 [20] Nielsen, C.V., Bicanic, N. (2003). Residual fracture energy of high-performance and normal  
472 concrete subject to high temperatures. *Materials and Structures*, 36, 515-521.
- 473 [21] Fares, H., Noumowe, A., Remond, S. (2009). Self-consolidating concrete subjected to high  
474 temperature Mechanical and physicochemical properties. *Cement and Concrete Research*, 39, 1230-  
475 1238.
- 476 [22] Ye, G., Liu, X., De Schutter, G., Taerwe, L., & Vandeveld, P. (2007). Phase distribution and  
477 microstructural changes of self-compacting cement paste at elevated temperature. *Cement and*  
478 *Concrete Research*, 37(6), 978-987.
- 479 [23] Tao, J., Liu, X., Yuan, Y., & Taerwe, L. (2013). Transient strain of self-compacting concrete  
480 loaded in compression heated to 700 C. *Materials and Structures*, 46(1-2), 191-201.
- 481 [24] Pistol, K., Weise, F., & Meng, B. (2013). High temperature behaviour of self-compacting  
482 concrete with limestone powder. In *Rheology and Processing of Construction Materials: Proceedings*  
483 *of the 7th RILEM International Conference on Self-Compacting Concrete and 1st RILEM*  
484 *International Conference on Rheology and Processing of Construction Materials*, RILEM  
485 *Proceedings PRO 90* (pp. 221-228). RILEM Bagnex.
- 486 [25] Dimitrios G. Aggelis, Tomoki Shiotani, Shouhei Momoki, and Akinobu Hiram (2009),  
487 *Acoustic Emission and Ultrasound for Damage Characterization of Concrete Elements*, *ACI*  
488 *Materials Journal*, 106(6), 1-6.
- 489 [26] ASTM E1316-17a: Standard Terminology for Nondestructive Examinations. ASTM  
490 International, Books of Standards, West Conshohocken, PA, 2017.
- 491 [27] Grosse, C.U., Ohtsu, M., *Acoustic emission testing*, Springer-Verlag Berlin Heidelberg, 2008.
- 492 [28] Sagar, R.V., Prasad, B.K.R. (2011). An experimental study on acoustic emission energy as a  
493 quantitative measure of size independent specific fracture energy of concrete beams. *Construction*  
494 *and Building Materials*, 25(5), 2349-2357.
- 495 [29] Dai, Q., NG, K., Zhou, J., Kreiger, E.L., Ahlborn, T.M. (2012). Damage investigation of single-  
496 edge notched beam tests with normal strength concrete and ultra high performance concrete  
497 specimens using acoustic emission techniques. *Construction and Building Materials*, 31, 231-242.
- 498 [30] Ohno, K., Uji, K., Ueno, A., Ohtsu, M. (2014). Fracture process zone in notched concrete beam  
499 under three-point bending by acoustic emission. *Construction and Building Materials*, 67, 139-145.
- 500 [31] Saliba, J., Loukili, A., Regoin, J.P., Grégoire, D., Verdon, L., Pijaudier-Cabot, G. (2015).  
501 Experimental analysis of crack evolution in concrete by the acoustic emission technique. *Frattura e*  
502 *Integrità Strutturale*, 34, 300-308.
- 503 [32] De Sutter, S., Verbruggen, S., Tysmans, T., Aggelis, D.G. (2017). Fracture monitoring of

- 504 lightweight composite-concrete beams. *Composite Structures*, 167, 11-19.
- 505 [33] Ohtsu, M., Uchida, M., Okamoto, T., and Yuyama, S. (2002). Damage Assessment of  
506 Reinforced Concrete Beams Qualified by Acoustic Emission. *ACI Structural Journal*, 99(4), 411-  
507 417.
- 508 [34] RILEM Technical Committee 212-ACD: Test method for damage qualification of reinforced  
509 concrete beams by acoustic emission. (2010). *Materials and Structures*, 43, 1183-1186.
- 510 [35] Ziehl, P., Ridge, A. (2006). Evaluation of strengthened RC beams: cyclic load test and acoustic  
511 emission methods. *ACI Structural Journal* 103(6), 832–41.
- 512 [36] Liu, Z., Ziehl, P. (2009). Evaluation of reinforced concrete beam specimens with acoustic  
513 emission and cyclic load test methods. *ACI Structural Journal* 106(3), 288–299.
- 514 [37] Colombo, S., Forde, M.C., Main, I.G., Shigeishi, M. (2005). Predicting the ultimate bending  
515 capacity of concrete beams from the “relaxation ratio” analysis of AE signals. *Construction and*  
516 *Building Materials* 19, 746–754.
- 517 [38] Schumacher, T., Higgins, C.C., Lovejoy, S.C. (2011). Estimating operating load conditions on  
518 reinforced concrete highway bridges with b-value analysis from acoustic emission monitoring.  
519 *Structural Health Monitoring*, 10(1), 17–32.
- 520 [39] Sagar R.V., Rao, M.V.M.S. (2014). An experimental study on loading rate effect on acoustic  
521 emission based b-values related to reinforced concrete fracture. *Construction and Building Materials*,  
522 70, 460–472.
- 523 [40] Zitto, M.E., Piotrkowski, R., Gallego, A., Sagasta, F., Benavent-Climent, A. (2015). Damage  
524 assessed by wavelet scale bands and b-value in dynamical tests of a reinforced concrete slab  
525 monitored with acoustic emission. *Mechanical Systems and Signal Processing*, 60, 75–89.
- 526 [41] Shiotani, T., Bisschop, J., Van Mier, J.G.M. (2003). Temporal and spatial development of  
527 drying shrinkage cracking in cement-based materials. *Engineering Fracture Mechanics*, 70, 1509–  
528 1525.
- 529 [42] Behnia, A., Chai, H.K., Shiotani, T. (2014). Advanced structural health monitoring of concrete  
530 structures with the aid of acoustic emission. *Construction and Building Materials*, 65, 282-302.
- 531 [43] Ohtsu, M., *Acoustic Emission (AE) and Related Non-destructive Evaluation (NDE) Techniques*  
532 *in the Fracture Mechanics of Concrete - Fundamentals and Applications*, Woodhead Publishing,  
533 Cambridge, 2015.
- 534 [44] Ohno, K., Ohtsu, M. (2010). Crack classification in concrete based on acoustic emission.  
535 *Construction and Building Materials*, 24, 2339-2346.
- 536 [45] Aggelis, D.G. (2011). Classification of cracking mode in concrete by acoustic emission  
537 parameters. *Mechanics Research Communications*, 38, 153–157.
- 538 [46] Farhidzadeh, A., Mpalaskas, A.C., Matikas, T.E., Farhidzadeh, H., Aggelis, D.G. (2014).  
539 Fracture mode identification in cementitious materials using supervised pattern recognition of  
540 acoustic emission features. *Construction and Building Materials*, 67, 129–138.
- 541 [47] Behnia, A., Chai, H.K., Yorikawa, M., Momoki, S., Terazawa, M., Shiotani, T. (2014).  
542 Integrated non-destructive assessment of concrete structures under flexure by acoustic emission and  
543 travel time tomography. *Construction and Building Materials*, 67, 202–215.

- 544 [48] Chen, B., Liu, J. (2004). Experimental study on AE characteristics of three-point-bending  
545 concrete beams. *Cement and Concrete Research*, 34(3), 391-397.
- 546 [49] Soulioti, D., Barkoula, N.M., Paipetis, A., Matikas, T.E., Shiotani, T., Aggelis, D.G. (2009).  
547 Acoustic emission behavior of steel fibre reinforced concrete under bending. *Construction and*  
548 *Building Materials*, 23(12), 3532-3536.
- 549 [50] Aggelis, D.G., Soulioti, D.V., Sapouridis, N., Barkoula, N., Paipetis, A., Matikas, T. (2011).  
550 Acoustic emission characterization of the fracture process in fibre reinforced concrete. *Construction*  
551 *and Building Materials*, 25(11), 4126-4131.
- 552 [51] Aggelis, D.G., Soulioti, D.V., Gatselou, E.A., Barkoula N.-M., Matikas, T.E. (2013).  
553 Monitoring of the mechanical behavior of concrete with chemically treated steel fibers by acoustic  
554 emission. *Construction and Building Materials*, 48, 1255–1260.
- 555 [52] Grosse, C., Ožbolt, J., Richter, R., Periškić, G. (2010). Acoustic emission analysis and thermo-  
556 hydro-mechanical model for concrete exposed to fire. *Journal of Acoustic Emission*, 28, 188-203.
- 557 [53] Ozawa, M., Uchida, S., Kamada, T., Morimoto, H. (2012). Study of mechanisms of explosive  
558 spalling in high-strength concrete at high temperatures using acoustic emission. *Construction and*  
559 *Building Materials*, 37, 621-628.
- 560 [54] Heap, M. L., Laumann, A., Hess, K.-U., Meredith, P., Dingwell, D., Huismann, S. (2013). The  
561 influence of thermal-stressing (up to 1000 °C) on the physical, mechanical, and chemical properties  
562 of siliceous-aggregate, high-strength concrete. *Construction and Building Materials*, 42, 248-465.
- 563 [55] Geng, J., Sun, Q., Zhang, W., Lü, C. (2016). Effect of high temperature on mechanical and  
564 acoustic emission properties of calcareous-aggregate concrete. *Applied Thermal Engineering*, 106,  
565 1200-1208.
- 566 [56] Xargay, H., Folino, P., Sambataro, L., Etse G. (2018). Temperature effects on failure behavior  
567 of self-compacting high strength plain and fiber reinforced concrete. *Construction and Building*  
568 *Materials*, 165, 723-734.
- 569 [57] Caggiano, A., Xargay, H., Folino, P., Martinelli, E. (2015). Experimental and numerical  
570 characterization of the bond behavior of steel fibers recovered from waste tires embedded in  
571 cementitious matrices. *Cement and Concrete Composites*, 62, 146-155.
- 572 [58] RILEM Technical Committee 162-TDF: Test and design methods for steel fibre reinforced  
573 concrete – Bending test. (2002). *Materials and Structures*, 35, 579-582.
- 574 [59] Caggiano, A., Gambarelli, S., Martinelli, E., Nisticò, N., Pepe, M. (2016). Experimental  
575 characterization of the post-cracking response in Hybrid Steel/Polypropylene Fiber-Reinforced  
576 Concrete. *Construction and Building Materials*, 125, 1035-1043.
- 577 [60] RILEM Technical Committee 50-FMC: Determination of fracture energy of mortar and  
578 concrete by means of three point bend tests on notched beams. (1985). *Materials and Structures*,  
579 18(106), 285-290.
- 580 [61] Pollock, A. (1989). Acoustic emission inspection, Technical report, TR-103-96-12/89, Physical  
581 Acoustics corporation, 195 Clarksville Road, Princeton Jct., NJ., USA.
- 582 [62] Rossi, P., Robert, J.L., Gervais, J.P. , Bruhat, D. (1989). Acoustic emission applied to study  
583 crack propagation in concrete. *Materials and Structures*, 22, 374-384.



- 584 [63] ACI Committee 224 - ACI 224R-01. (2001). Control of cracking in concrete structures.  
585 Reported by ACI Committee 244.
- 586 [64] RILEM Technical Committee 212-ACD: Test method for classification of active cracks in  
587 concrete structures by acoustic emission. (2010). Materials and Structures, 43, 1187-1189.
- 588 [65] WIRAND® FS3N, Steel fibres for concrete, Maccaferri Technical Data Sheet, 2010
- 589 [66] FIBROMAC12®, Mono-filamentary polypropylene fibre, Maccaferri Technical Data Sheet,  
590 2010.
- 591

592

593

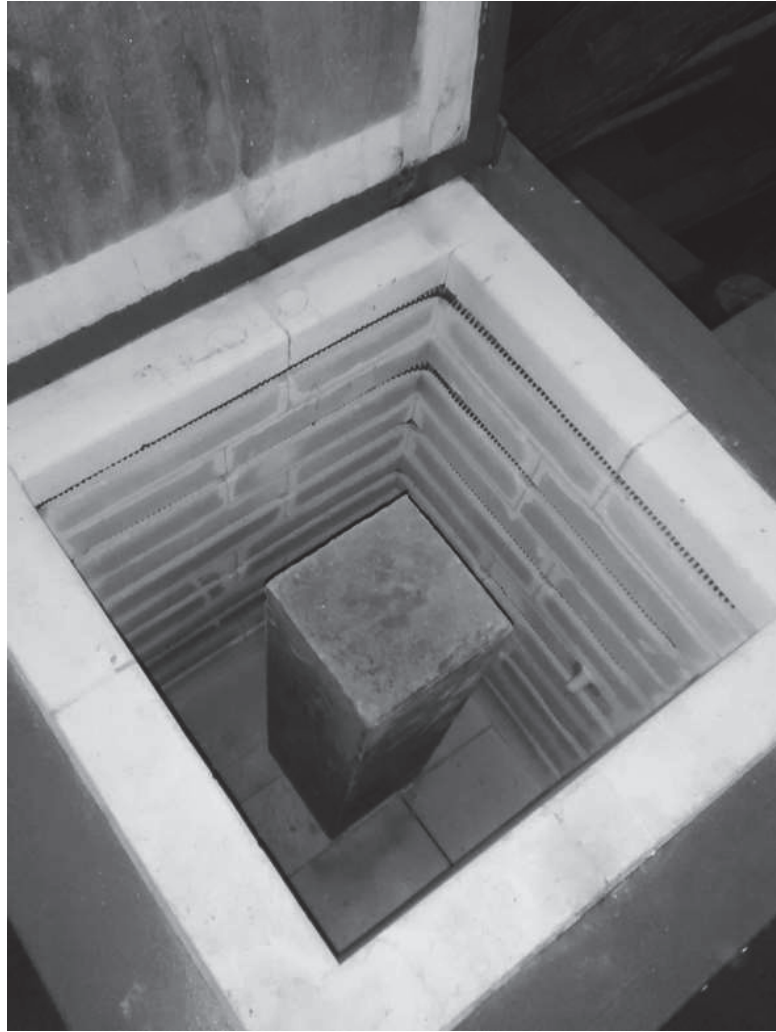


594

595

*Figure 1: Hooked-end steel macrofibers and polypropylene microfibers.*

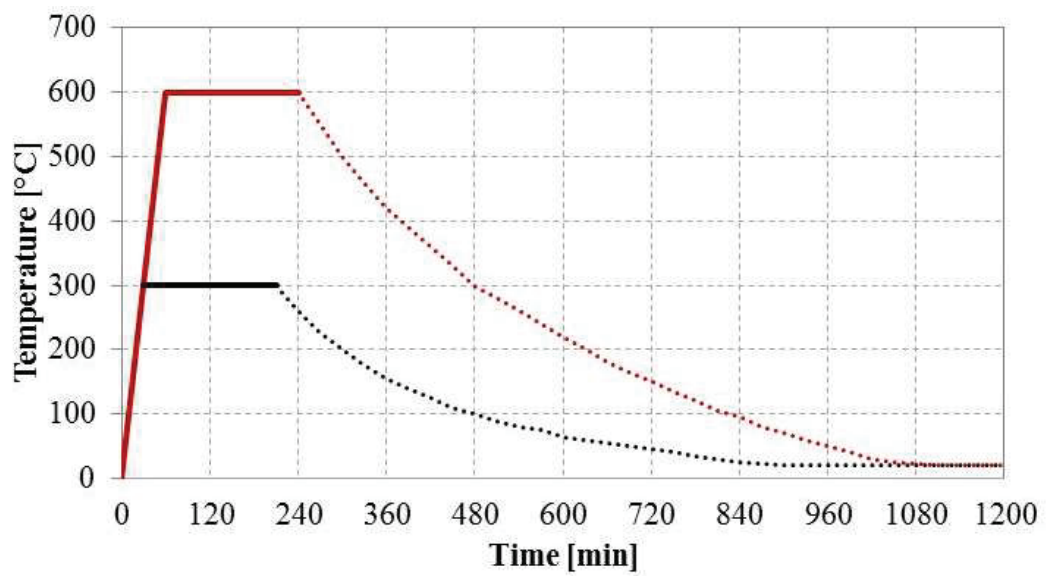
596



597

598

(a)



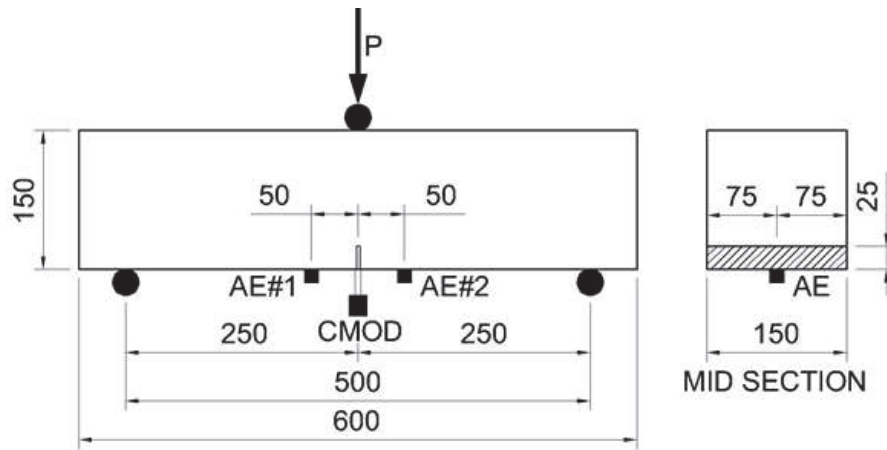
599

600

601

(b)

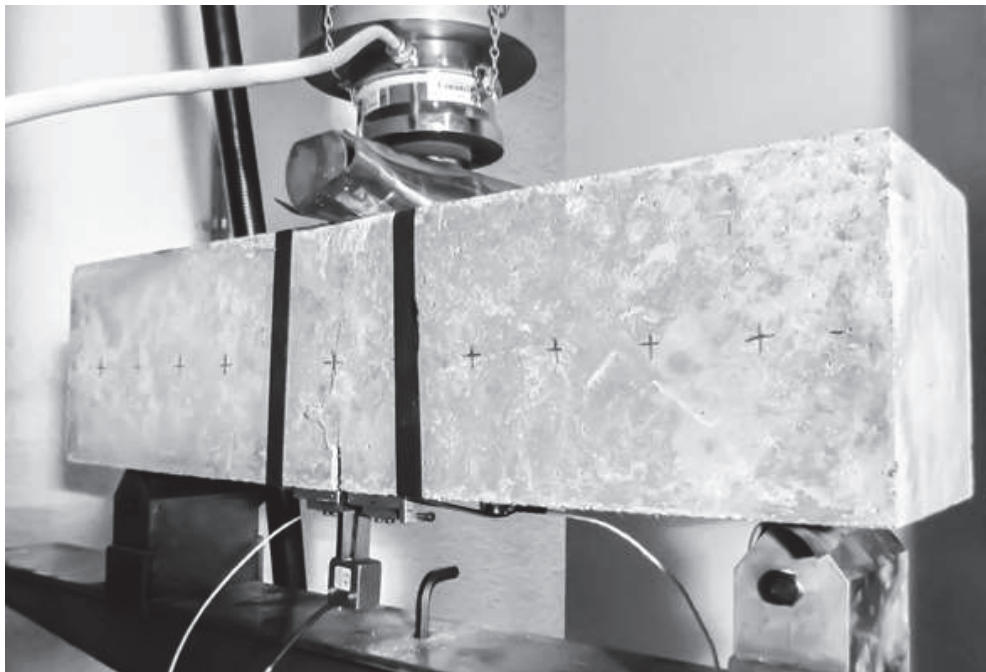
Figure 2: (a) Electric furnace and (b) heating curve.



602

603

(a)



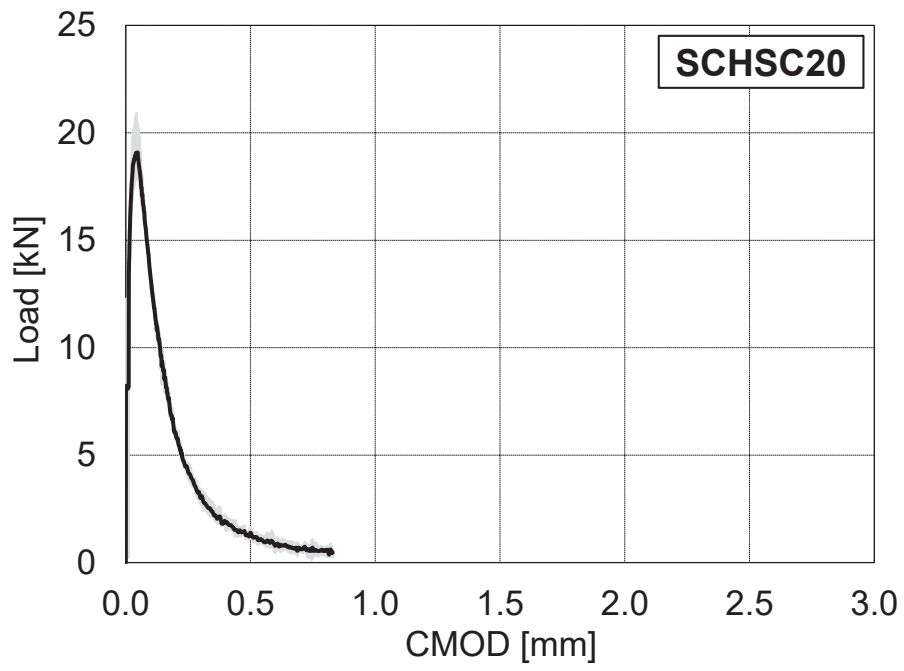
604

605

(b)

606 *Figure 3: Three-point bending test setup: (a) beam geometry (distances in mm) and (b) sensors*  
 607 *arrangement.*

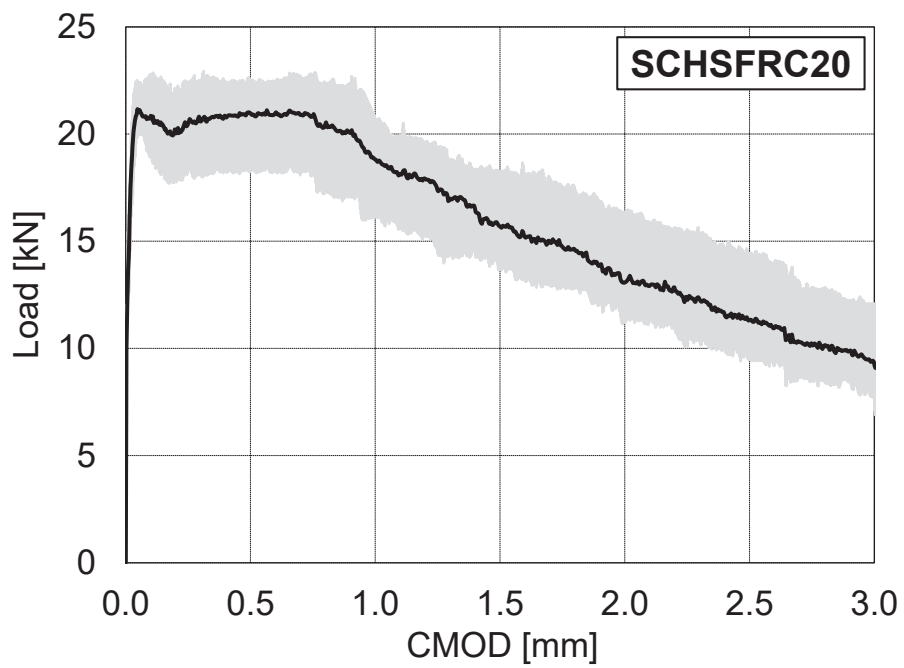
608



609

610

(a)



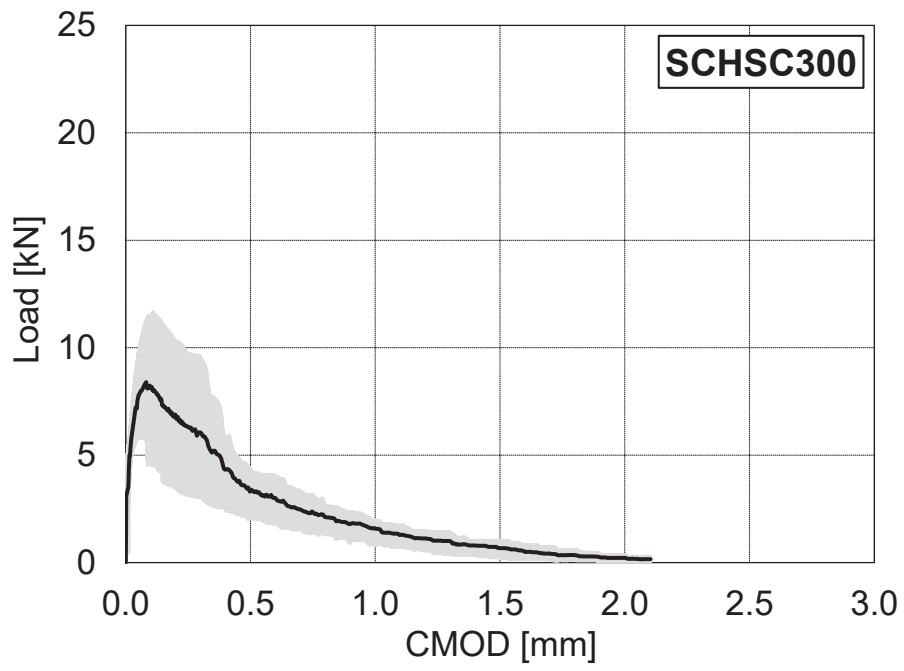
611

612

(b)

613

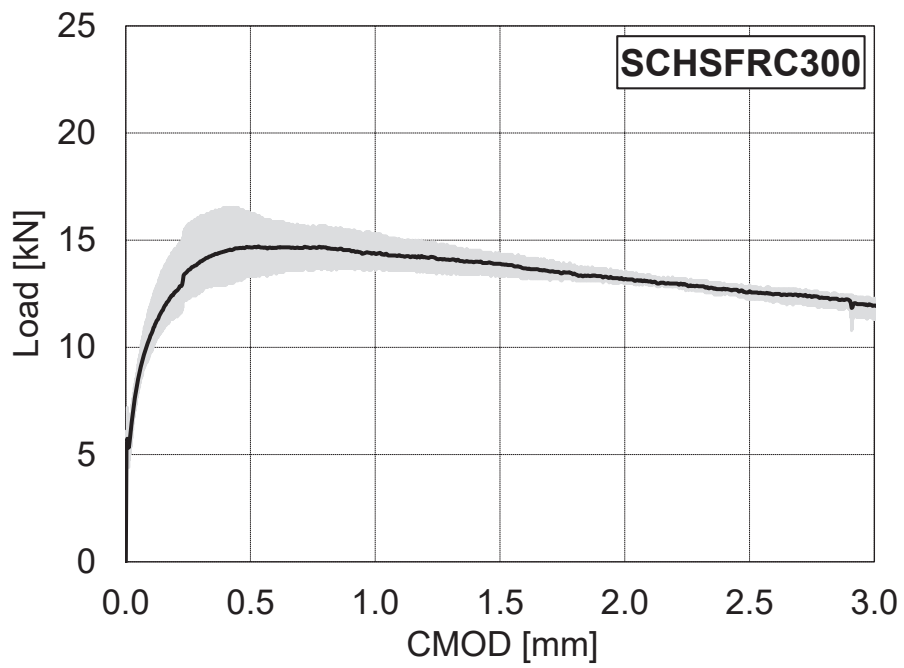
Figure 4: Load vs CMOD at reference temperature (20 °C): (a) SCHSC and (b) SCHSFRC.



614

615

(a)



616

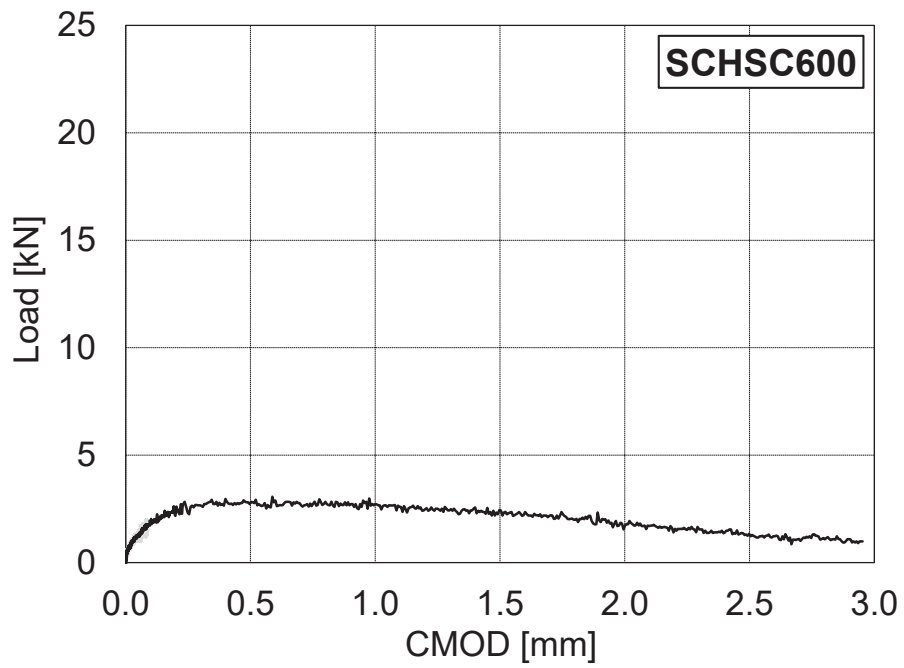
617

(b)

618

Figure 5: Residual Load vs CMOD curve after 300°C: (a) SCHSC and (b) SCHSFRC.

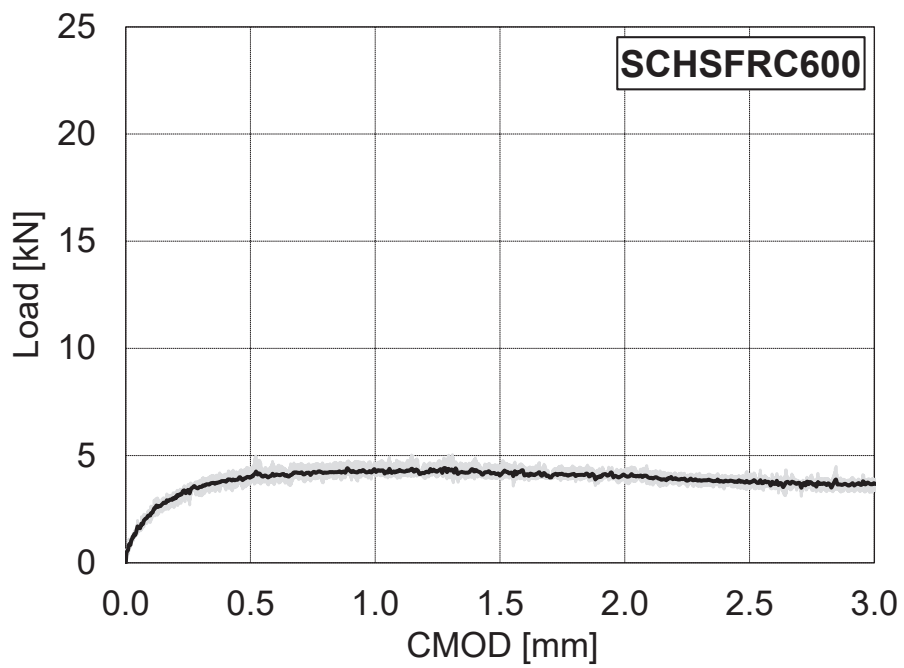
619



620

621

(a)



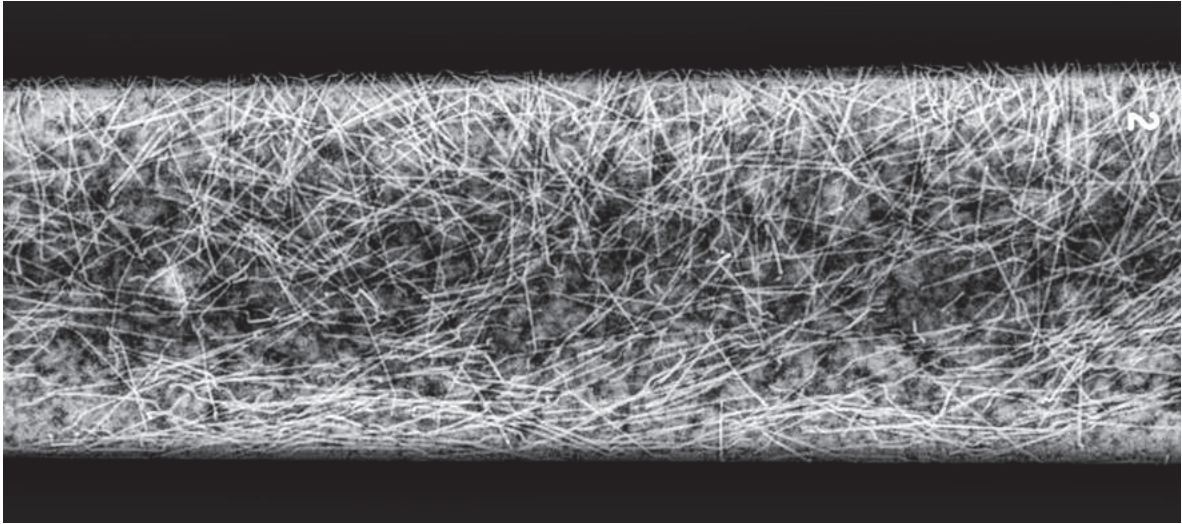
622

623

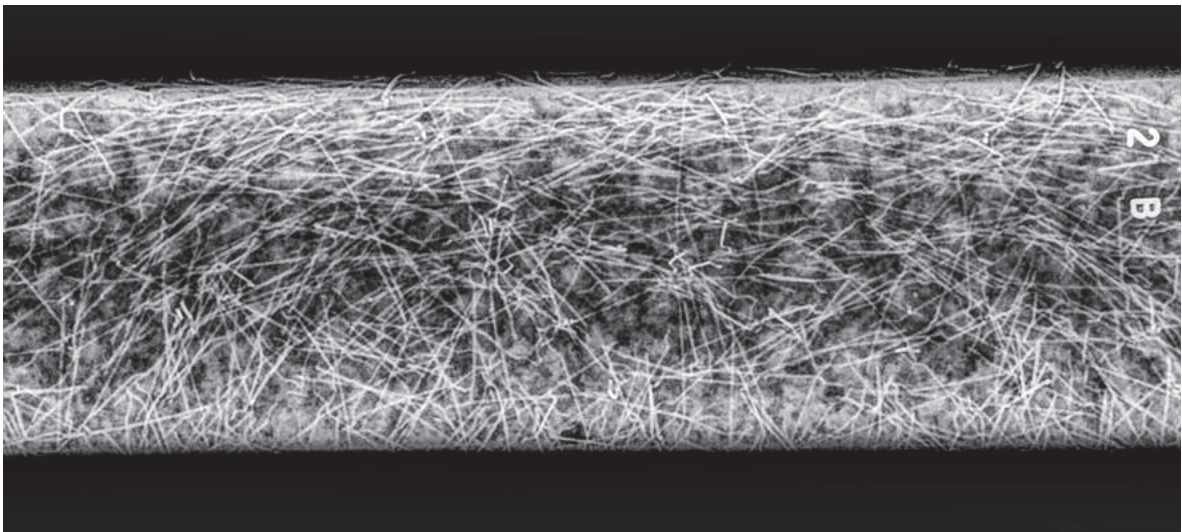
(b)

624 *Figure 6: Residual Load vs CMOD curve after 600°C: (a) SCHSC and (b) SCHSFRC. Only one test*  
 625 *for SCHSC600 was stably completed.*

626



627



628

629 *Figure 7: X-ray images showing distribution of steel fibers in the same concrete sample and rotated*  
630 *90 degrees.*

631





632

633

(a)



634

635

(b)



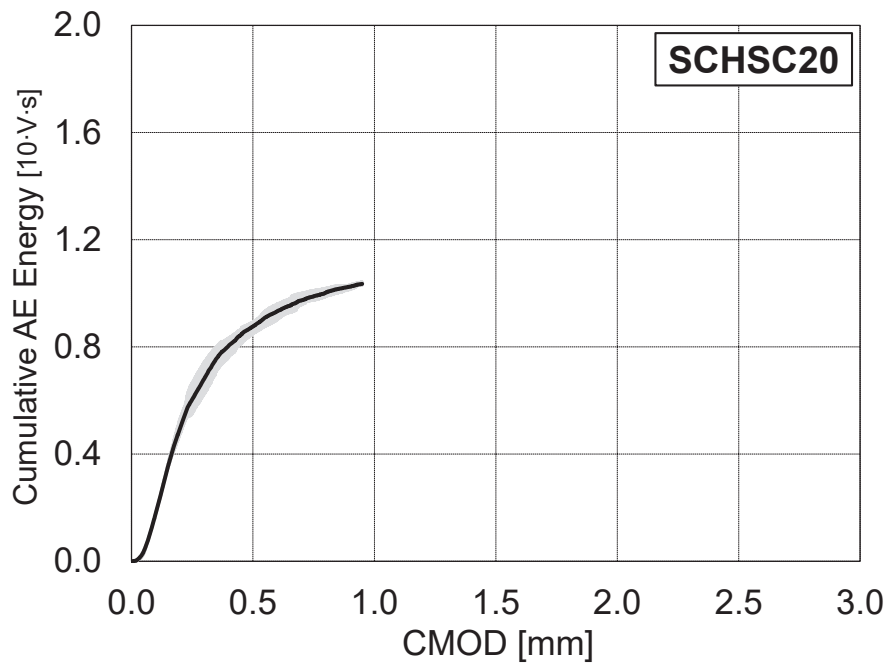
636

637

(c)

638 *Figure 8: (a) Fracture surface aspect of SCHSC, crack patterns of (b) SCHSC and (c) SCHSFRC.*

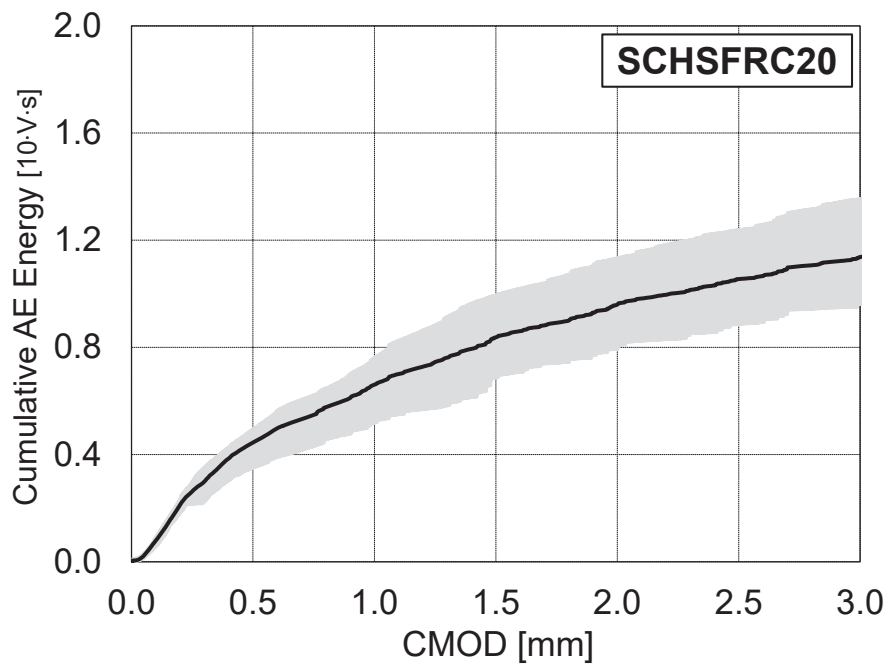
639



640

641

(a)



642

643

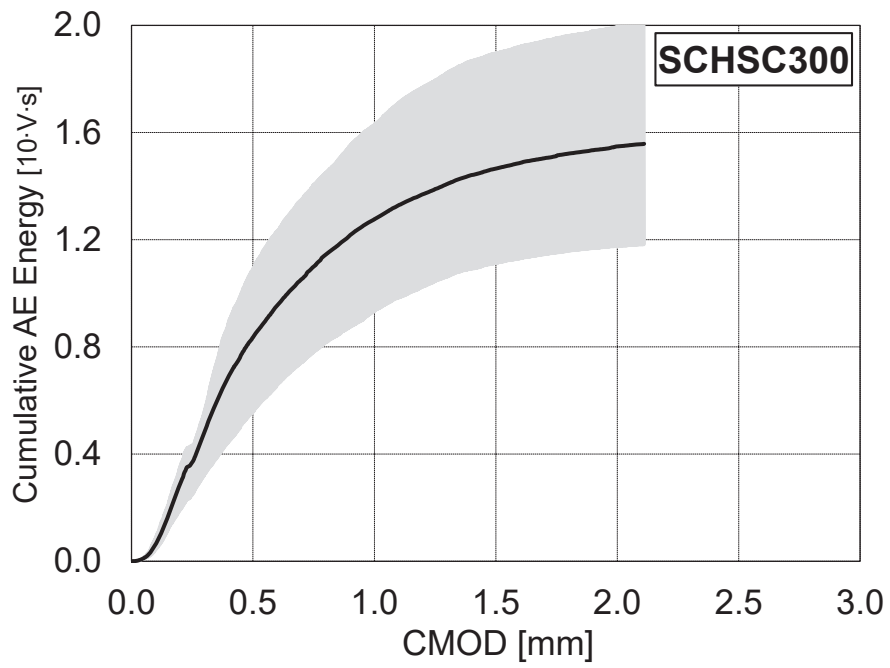
(b)

644 *Figure 9: Cumulative AE Energy parameter vs CMOD at reference temperature (20 °C): (a)*

645

*SCHSC and (b) SCHSFRC.*

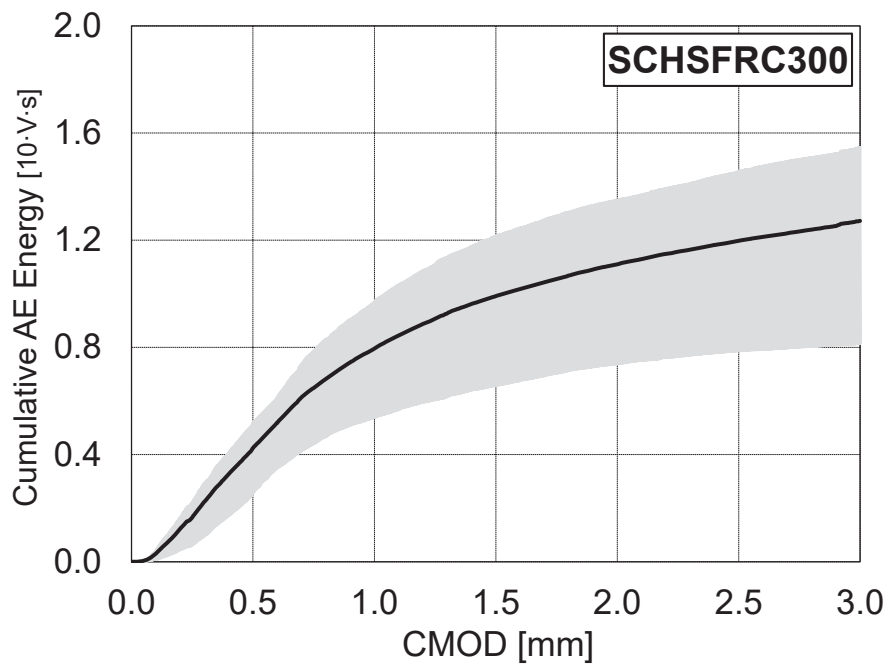
646



647

648

(a)



649

650

(b)

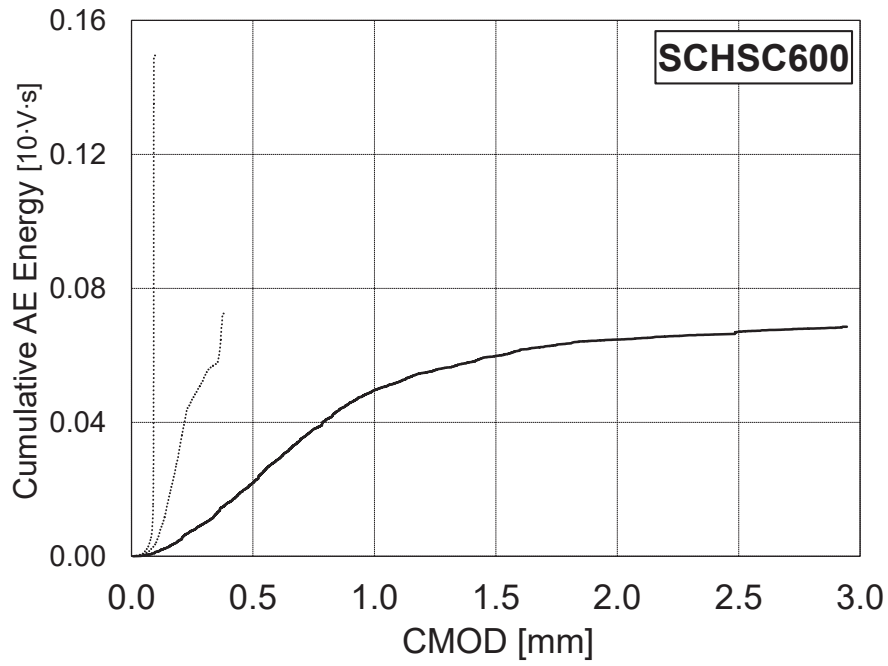
651

Figure 10: Cumulative AE Energy parameter vs CMOD after 300°C: (a) SCHSC and (b)

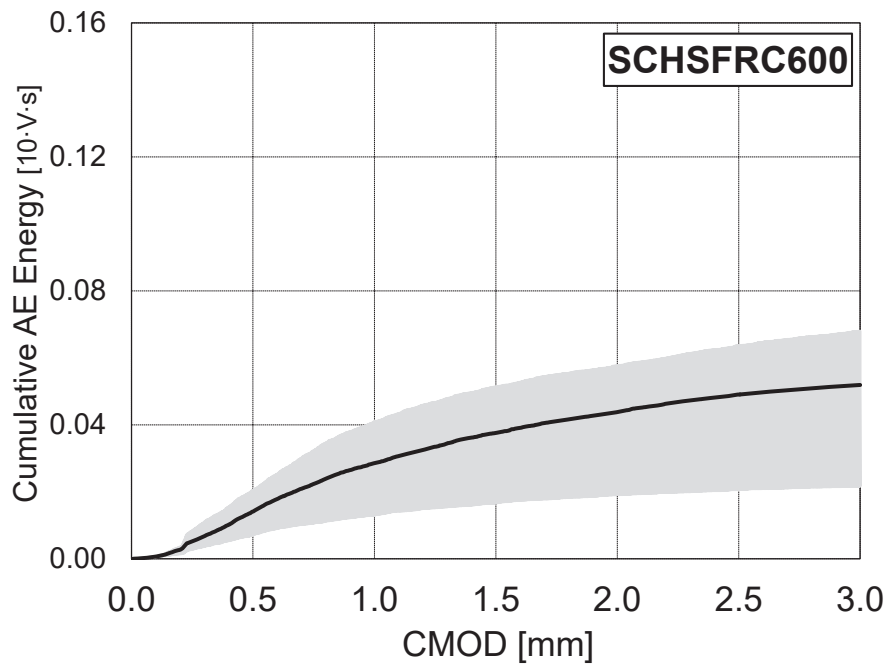
652

SCHSFRC.

653



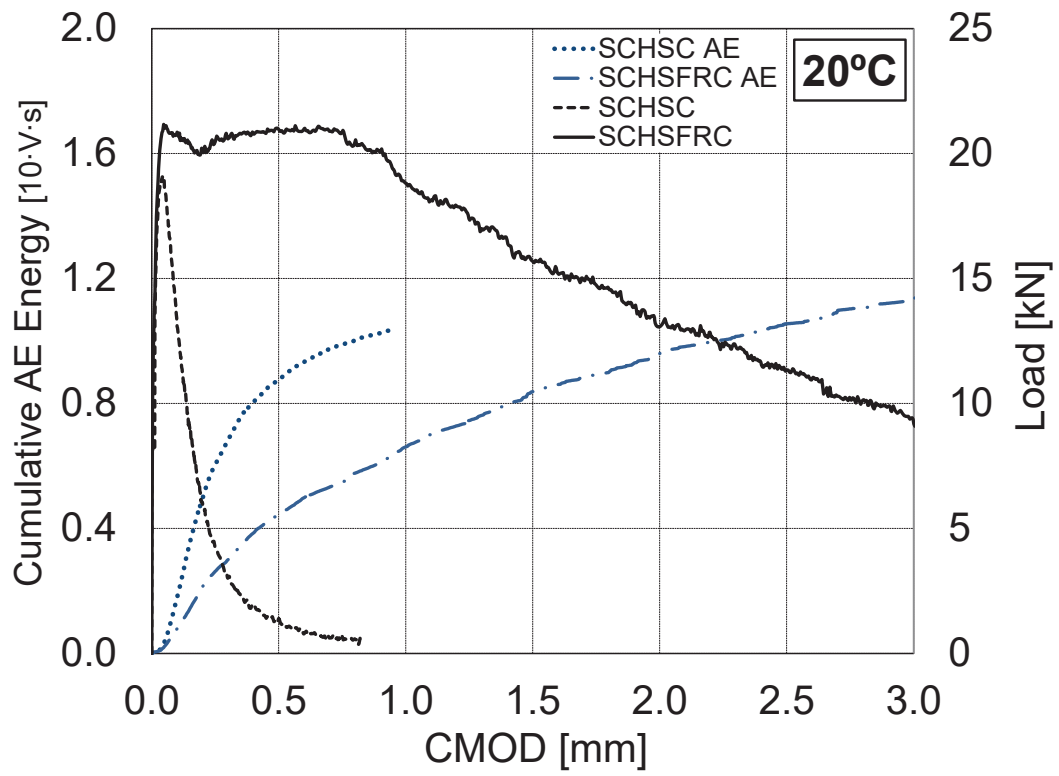
(a)



(b)

658 *Figure 11: Cumulative AE Energy parameter vs CMOD after 600°C: (a) SCHSC and (b)*  
 659 *SCHSFRC.*

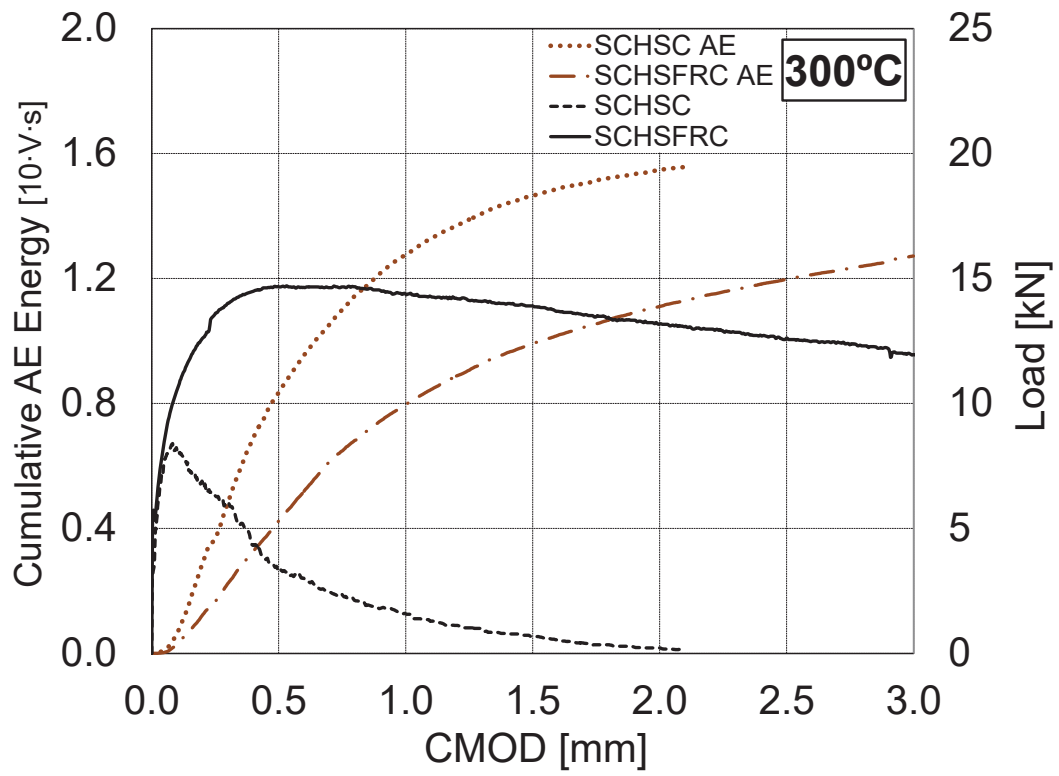
660



661

662 *Figure 12: Load and cumulative AE Energy vs CMOD behavior at reference temperature.*

663

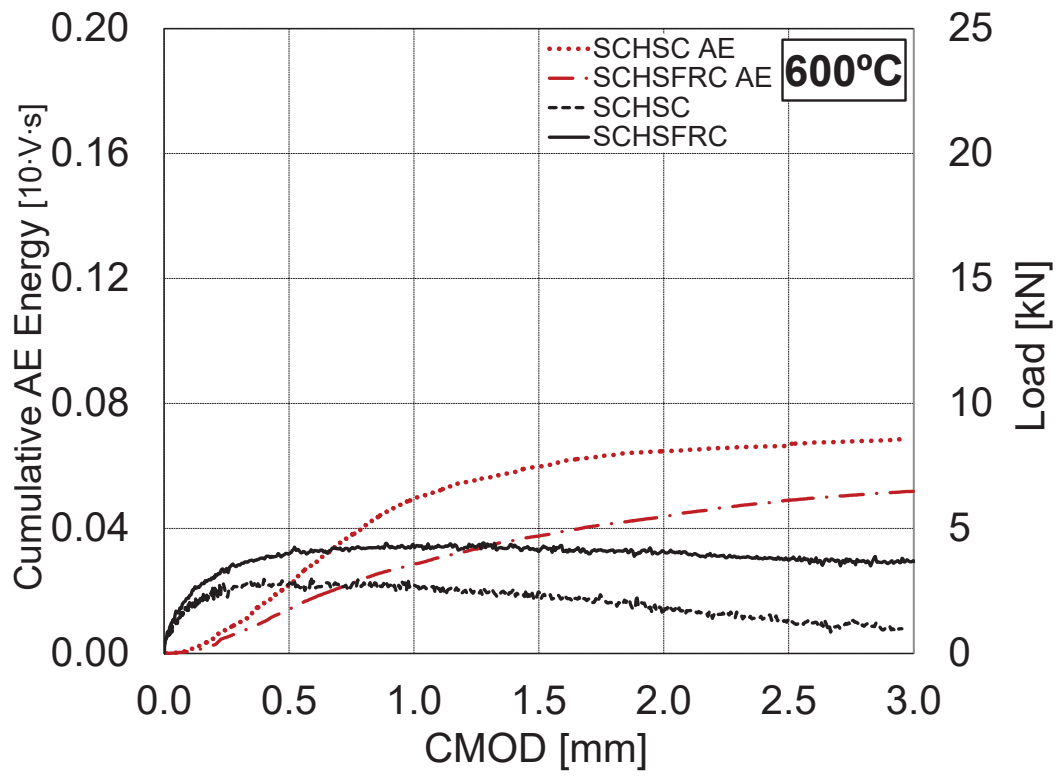


664

665

Figure 13: Load and cumulative AE Energy vs CMOD residual behavior after 300°C.

666



667

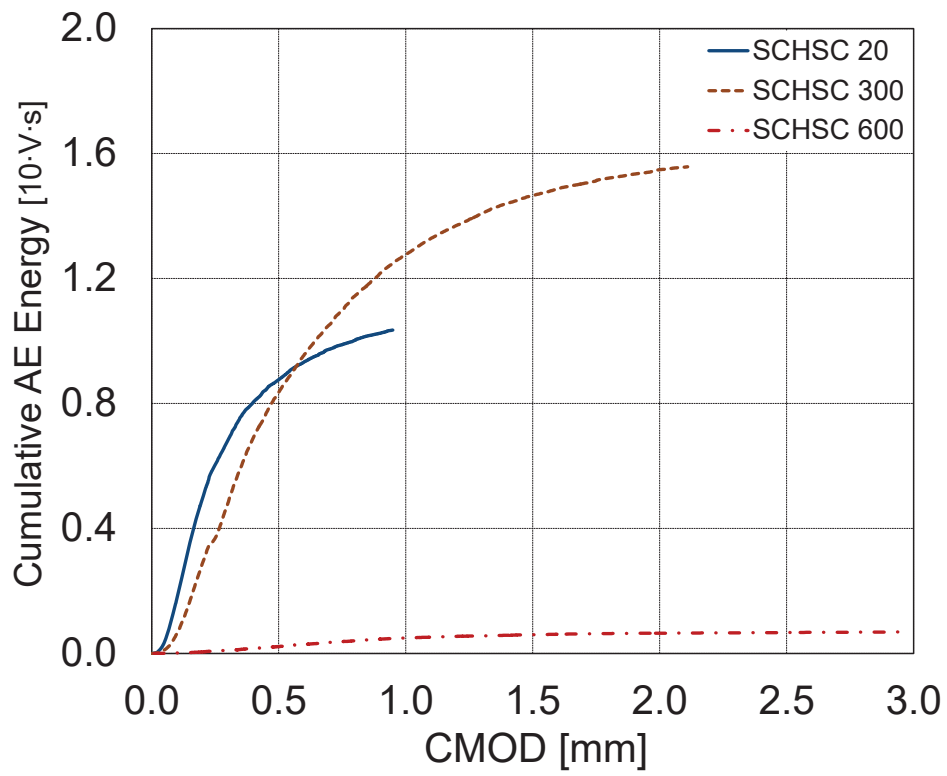
668 *Figure 14: Load and cumulative AE Energy vs CMOD residual behavior after 600°C. AE data was*

669

*intentionally rescaled.*

670



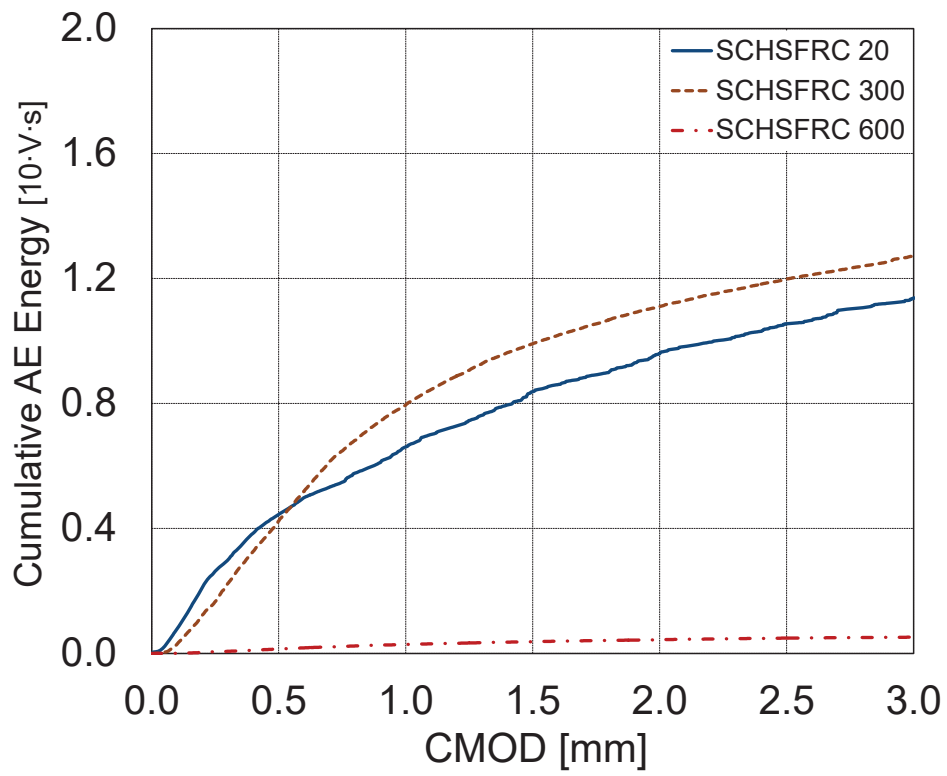


671

672

*Figure 15: Cumulative AE energy vs CMOD: SCHSC specimens.*

673

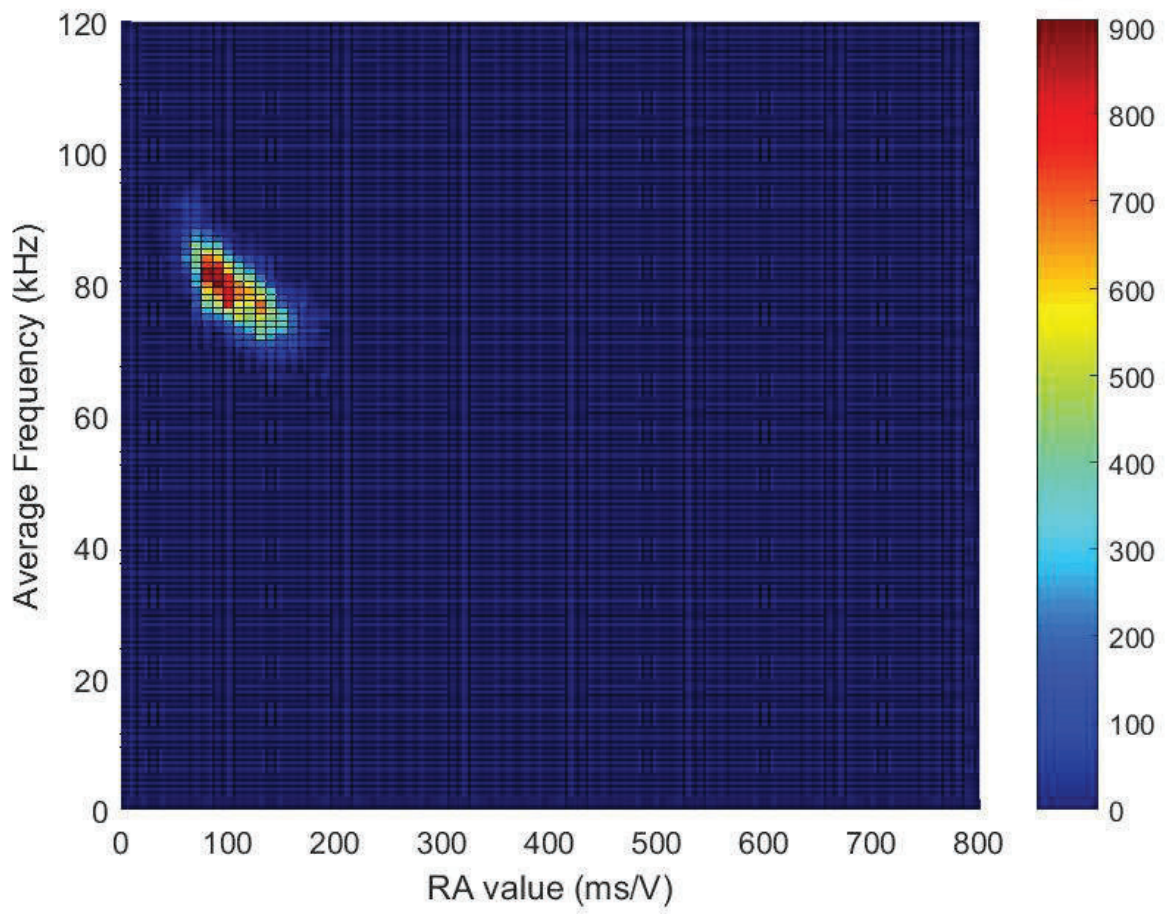


674

675

Figure 16: Cumulative AE energy vs CMOD: SCHSFRC specimens.

676

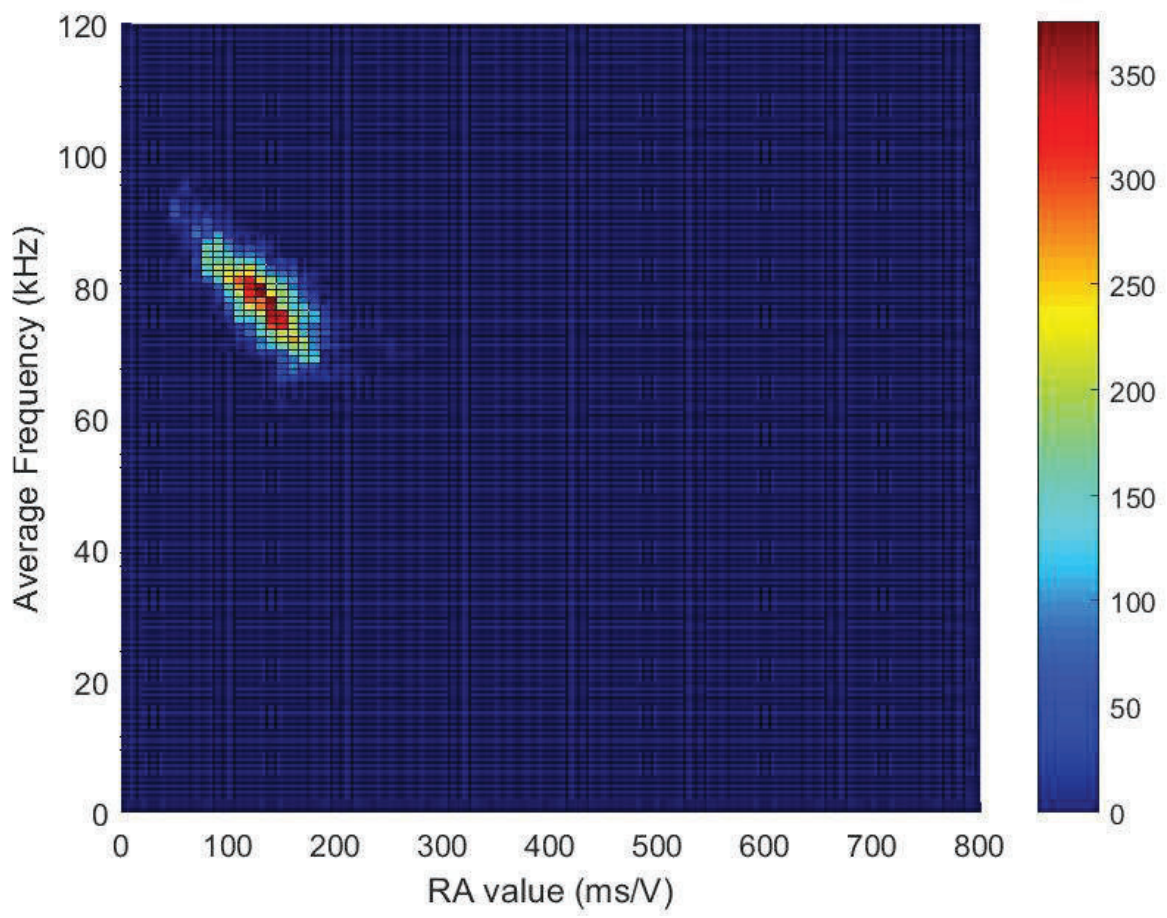


677

678

679

(a)

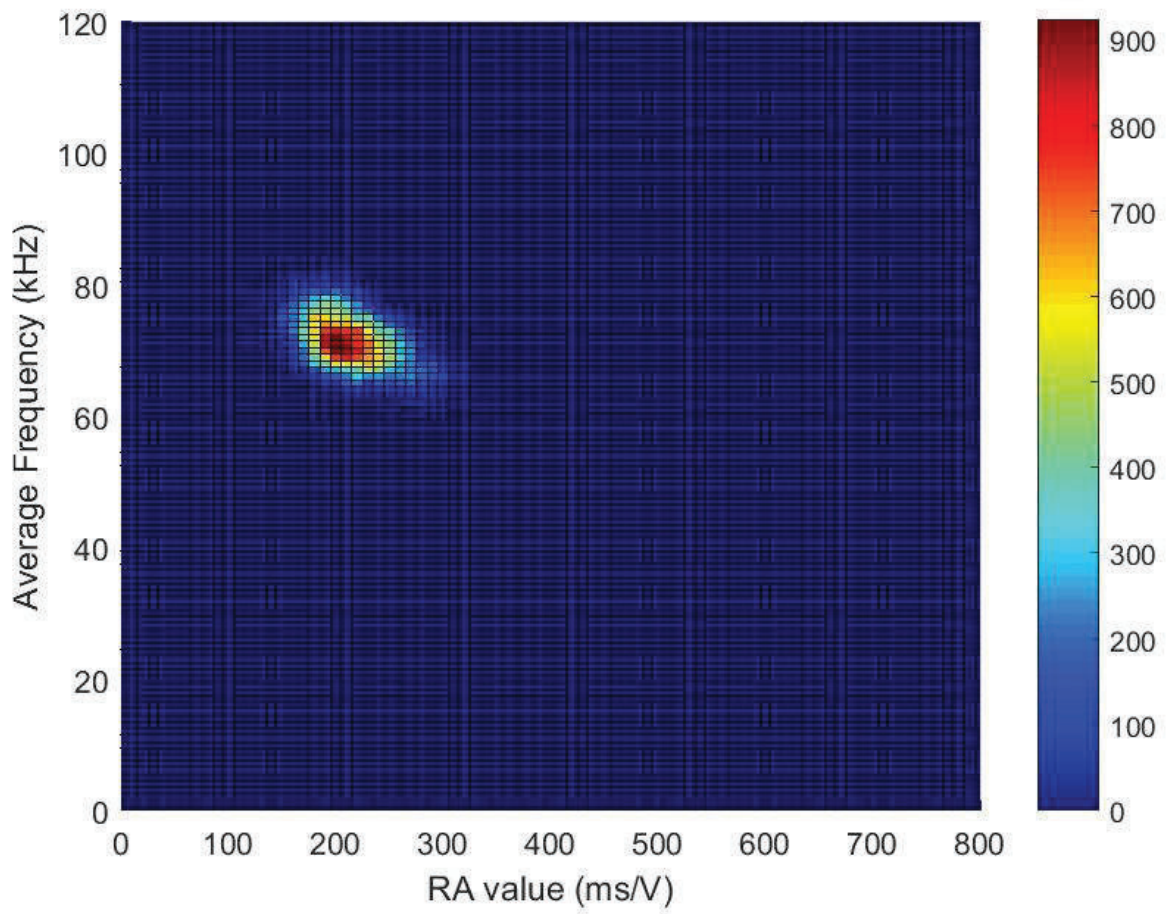


680

681

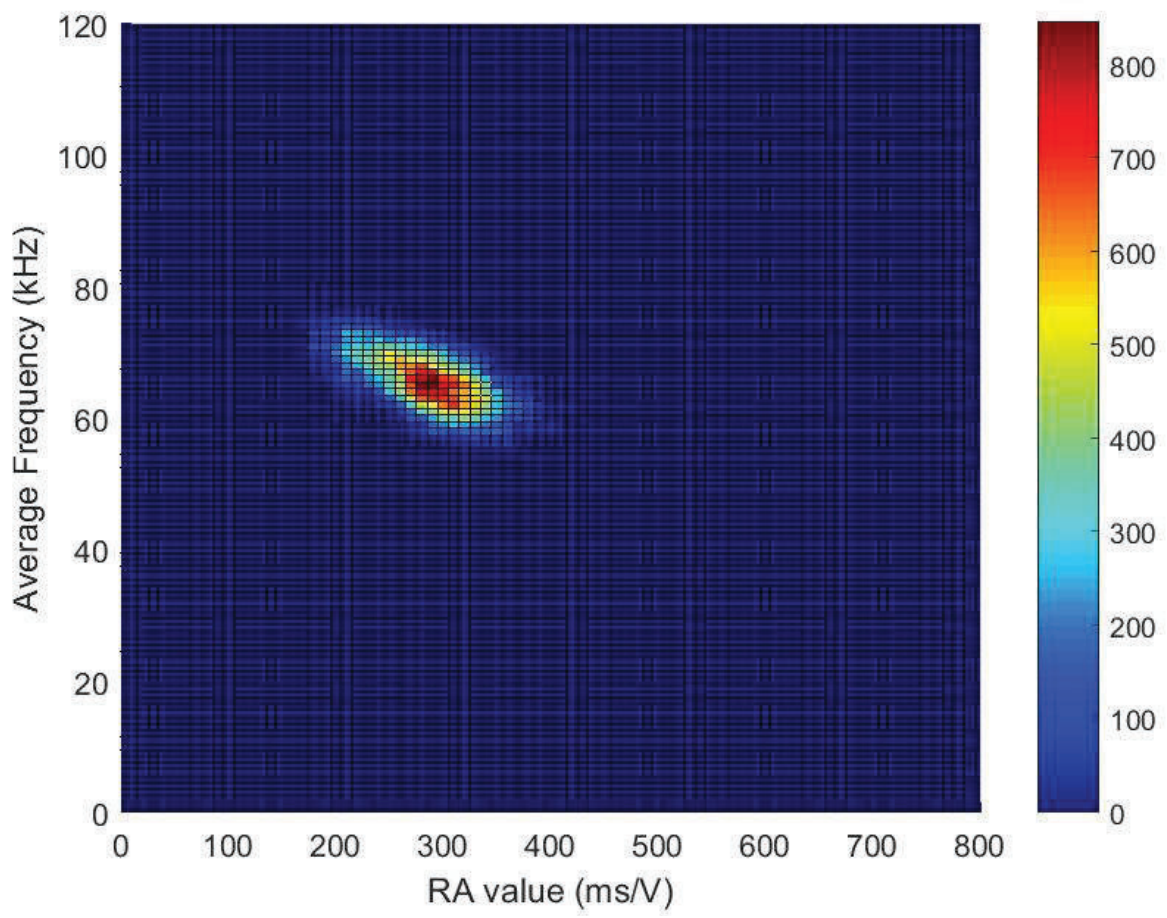
682

(b)



683  
684  
685

(c)

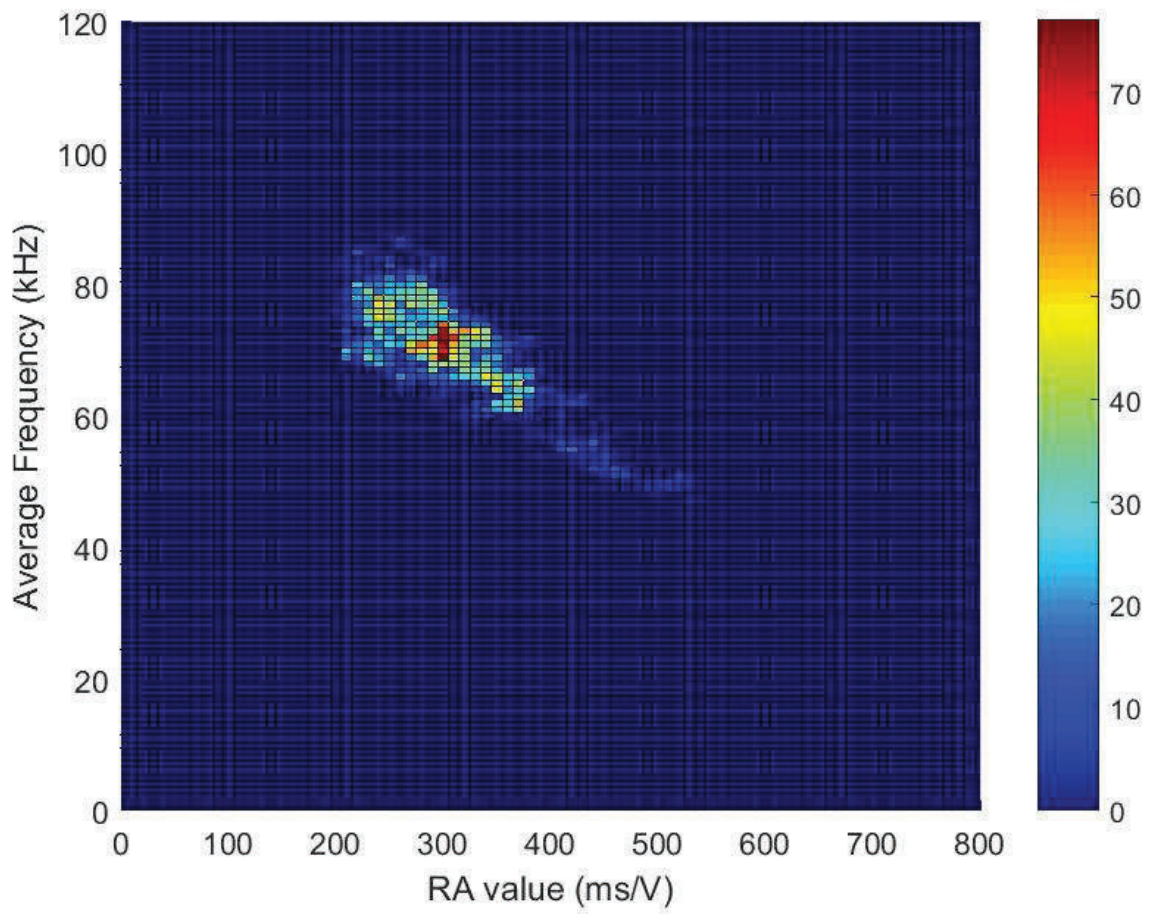


686

687

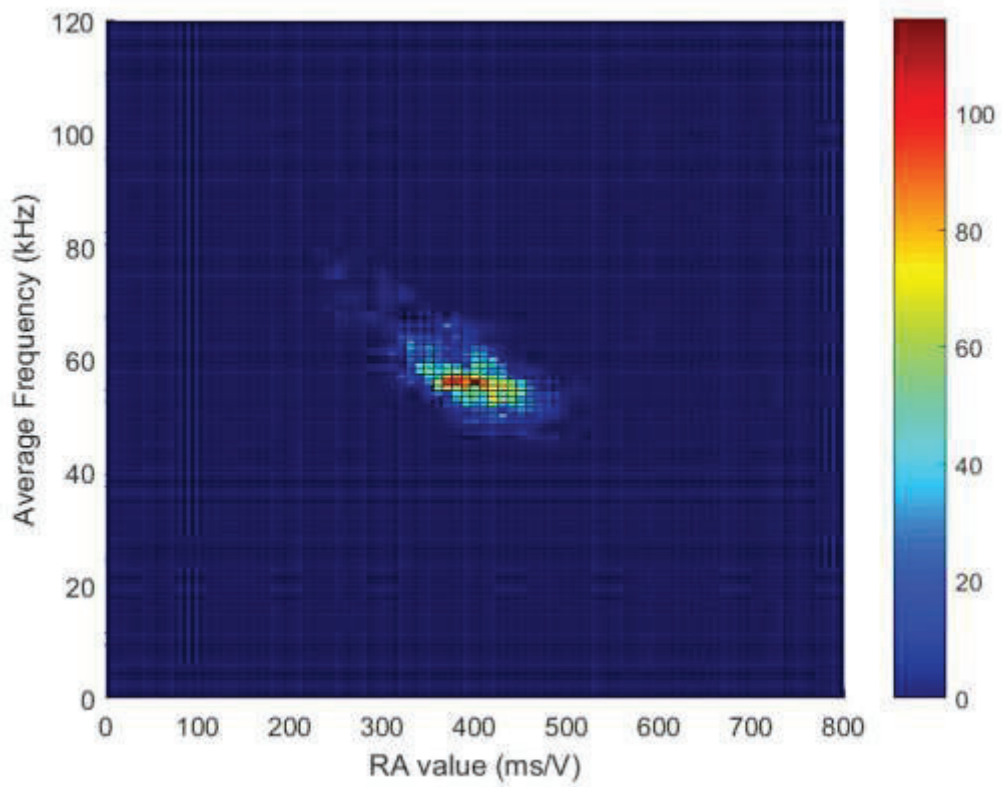
688

(d)



689  
690  
691

(e)



692

693

(f)

694

*Figure 17: 2D histogram of RA value – Average frequency for specimens corresponding to (a)*

695

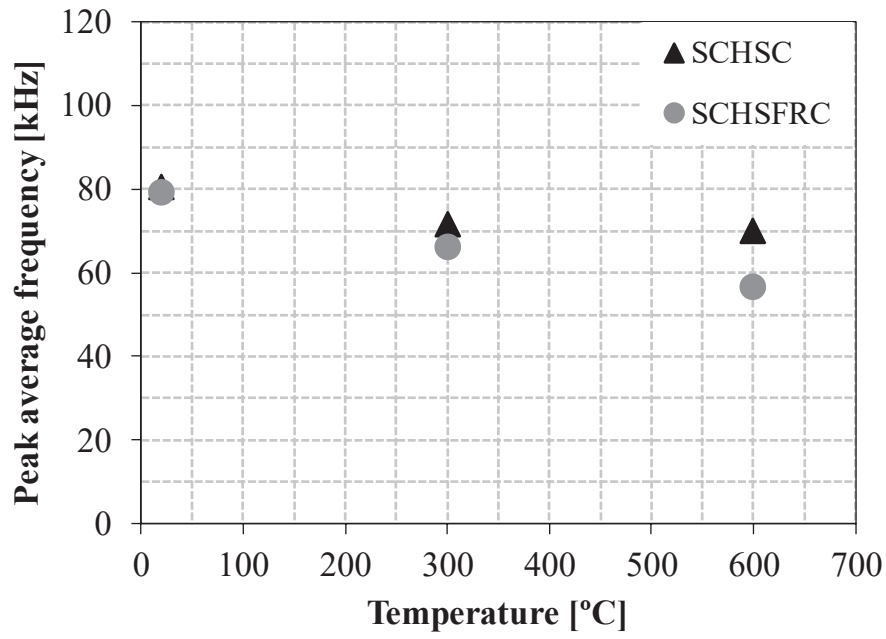
*SCHSC20, (b) SCHSFRC20, (c) SCHSC300, (d) SCHSFRC300, (e) SCHSC600, and (f)*

696

*SCHSFRC600.*

697

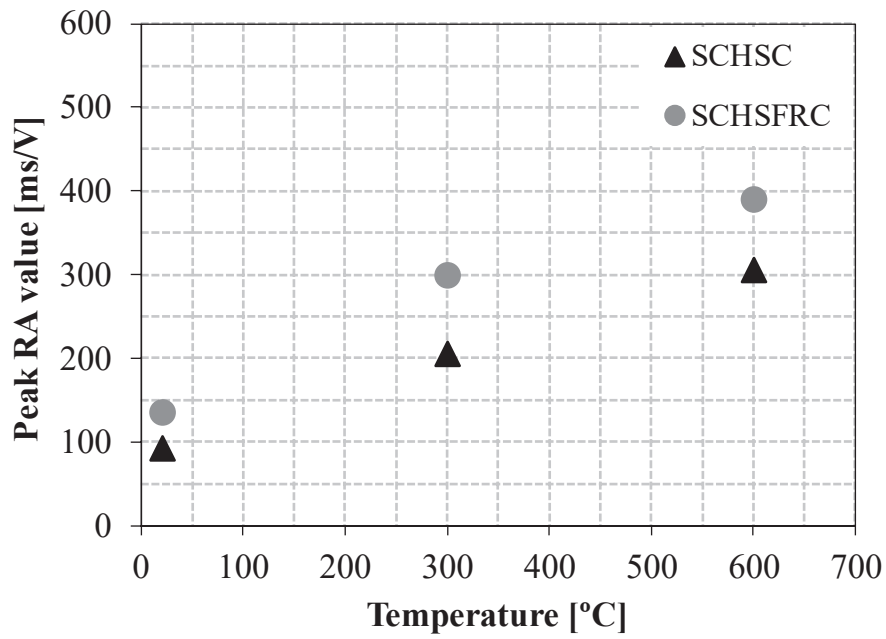




698

699

(a)



700

701

(b)

702 *Figure 18: Temperature evolutions of (a) Peak frequency distribution of AF and (b) Peak frequency*  
 703 *distribution of RA value.*

704

705

706

707 *Table 1: Basic mixture composition per cubic meter.*

| Materials                 | Dosage<br>[kg/m <sup>3</sup> ] |
|---------------------------|--------------------------------|
| Cement                    | 429.8                          |
| GGBFS                     | 183.9                          |
| Water                     | 214.6                          |
| Natural fine sand         | 281.1                          |
| Crushed sand              | 499.7                          |
| Crushed coarse aggregates | 783.7                          |
| Superplasticizer          | 3.1                            |

708

709 *Table 2: Fibers main technical data [65][66].*

| Fibers        | Diameter<br>[mm] | Length<br>[mm] | Tensile Strength<br>[MPa] | Elastic Modulus<br>[GPa] | Specific weight<br>[kN/m <sup>3</sup> ] | Content<br>[kg/m <sup>3</sup> ] |
|---------------|------------------|----------------|---------------------------|--------------------------|---|---------------------------------|
| Steel         | 0.75             | 33             | 1100                      | 200                      | 78.5                                    | 60                              |
| Polypropylene | 0.032            | 12             | 400-500                   | 3.5-3.9                  | 9.1                                     | 0.9                             |

710

711 *Table 3: Flexural parameters of the different mixtures after exposed to temperature according to*  
 712 *RILEM TC 162-TDF and 50-FMC.*

| Concrete Mixture | $F_L$<br>[kN] | $f_{fct,L}$<br>[MPa] | $f_{max}$<br>[MPa] | $G_f$<br>[N/m] | $D_{BZ}^b$<br>[Nmm] | $D_{BZ,2}^f$<br>[Nmm] | $D_{BZ,3}^f$<br>[Nmm] | $f_{eq,2}$<br>[MPa] | $f_{eq,3}$<br>[MPa] | $f_{R,1}$<br>[MPa] | $f_{R,2}$<br>[MPa] | $f_{R,3}$<br>[MPa] |
|------------------|---------------|----------------------|--------------------|----------------|---------------------|-----------------------|-----------------------|---------------------|---------------------|--------------------|--------------------|--------------------|
| SCHSC20          | 19.1          | 6.1                  | 6.1                | 202            | 3672                | -                     | -                     | -                   | -                   | -                  | -                  | -                  |
| SCHSFRC20        | 21.1          | 6.7                  | 6.7                | -              | 3834                | 12004                 | 45091                 | 7.7                 | 5.8                 | 6.7                | 5.0                | 3.6                |
| SCHSC300         | 8.2           | 2.6                  | 2.6                | 290            | 4931                | -                     | -                     | -                   | -                   | -                  | -                  | -                  |
| SCHSFRC300       | 8.5           | 2.7                  | 4.7                | -              | 2285                | 8009                  | 39285                 | 5.1                 | 5.0                 | 4.7                | 4.4                | 4.0                |
| SCHSC600         | 1.3           | 0.4                  | 0.8                | 133            | 2206                | -                     | -                     | -                   | -                   | -                  | -                  | -                  |
| SCHSFRC600       | 1.7           | 0.5                  | 1.4                | -              | 511                 | 2129                  | 11567                 | 1.4                 | 1.5                 | 1.3                | 1.3                | 1.2                |

713